THESIS FOR THE DEGREE OF DOCTOR OF PHILOSOPHY

Influence of combined thermal and mechanical loadings on pearlitic steel microstructure in railway wheels and rails

DIMITRIOS NIKAS

Department of Industrial and Materials Science
CHALMERS UNIVERSITY OF TECHNOLOGY
Gothenburg, Sweden 2018

Influence of combined thermal and mechanical loadings on pearlitic steel microstructure in railway wheels and rails
DIMITRIOS NIKAS
ISBN 978-91-7597-801-7

Doktorsavhandlingar vid Chalmers tekniska högskola
Ny serie nr. 4482
ISSN 0346-718X
Department of Industrial and Materials Science
Chalmers University of Technology
SE-412 96 Gothenburg
Sweden
Telephone: +46 (0)31-772 1000

Cover:
TEM micrograph of R260 rail steel with alternating ferrite and cementite lamellae, where the black arrows show examples of dislocations in the ferrite lamellae.

Printed by Chalmers Reproservice
Gothenburg, Sweden 2018

Influence of combined thermal and mechanical loadings on pearlitic steel microstructure in railway wheels and rails

DIMITRIOS NIKAS
Department of Industrial and Materials Science
Chalmers University of Technology

Abstract

One of the most important aspects in railway operation is the interaction between rail and wheel. The contact patch between these two components is around the size of a small coin, and since high loads act on this small area, stresses will give rise to wear and damage on both components. Frictional forces in the surface of wheels and rails caused by recurring train acceleration, braking, curving and occasional slippage can cause cyclic plastic deformation and heating, which in turn causes an aligned, anisotropic microstructure with altered mechanical behaviour. Control of material property degradation is an important topic for guiding maintenance, as well as ensuring safety, reliability and sustainability of railways, since it will allow for a more accurate prediction of material wear and lifetime.

The thesis focuses on the mechanical properties of railway wheel and rail steels after exposure to elevated temperatures and plastic deformation. Specifically examined are the carbon wheel steels, UIC ER7T and ER8T (∼0.55 wt.% C) and rail steel R260 (∼0.72 wt% C). During their service life, the surface layers of rails and wheels are subjected to very high rolling contact loads. These lead to accumulation of large shear strains close to the running surface. Moreover the high thermal loads that wheels experience when block brakes are used can cause severe degradation of the material microstructure, more specifically spheroidisation of the pearlite, which combined with plastic deformation (that makes the material more prone to spheroidisation) can lead to severe deterioration of the material's mechanical properties. Both un-deformed and pre-strained wheel materials were heat treated at various temperatures from 250°C to 600°C for various durations, and the change in room temperature hardness was analysed. Additionally, Electron Backscatter Diffraction Analysis (EBSD) was used to evaluate if orientation gradients in the pearlitic colonies affect the spheroidisation of the pearlitic microstructure, that is observed at higher temperatures. Uniaxial (tension-compression) and biaxial (including torsion) low cycle fatigue tests were performed to study the behaviour of R7T and R8T material at different temperatures. The influence of hold times as well as the ratcheting behaviour with mean stress effects were also studied. Virgin rail material was twisted using a biaxial machine to various shear strain levels to create a microstructure representative for the surface layer observed in field samples. The microstructure was characterised using scanning electron microscopy (SEM), transmission electron microscopy (TEM) and hardness measurements.

The results showed that wheel material hardening due to strain ageing takes place at around 300°C, while microstructural degradation caused softening at higher temperatures. Spheroidisation of the pearlite started to become visible at 450°C for the un-deformed material and at around 400°C for the pre-strained. The spheroidised areas appear to have lost their initial orientation gradients after spheroidisation, and obtain a more uniform orientation. Cyclic tests at elevated temperature revealed cyclic hardening at around 300°C, as an effect of dynamic strain ageing. At higher temperatures, cyclic softening

followed due to a combination of increasing thermal activation and spheroidisation. Biaxial testing showed a more severe effect of strain hardening and shorter fatigue life. For the rail material, the dislocation density was found to increase with increasing shear strain. The flow stresses calculated using microstructural parameters such as dislocation density and interlamellar spacing of the pearlite seem to agree well with those evaluated from hardness measurements.

Keywords: Low cycle fatigue (LCF); Multiaxial fatigue; Hardness; Thermal effects; Spheroidisation; Pearlite; Wheel steels; Rail steels; EBSD; TEM;

To Evangelia and my family back in Greece for all the support through the years.

If it's worth having you can't have it now. Or tomorrow. You must work for it. Patiently.

/

When you reach the goal, when you hit the target, it will have been worth it. On that day you will believe in time, in volume, in repetition and practice.

/

And you will be happy that it didn't come easily. I promise.

Mark Twight

Preface

The research presented in this doctoral thesis is based on the work performed on the project MU28 within the National Centre of Excellence CHARMEC (Chalmers Railway Mechanics). Part of the work financed within the European Horizon 2020 Joint Technology Initiative Shift2Rail through contract No. 730841. The experimental work presented in this thesis has been performed at the department of Industrial and Materials Science (previously Materials and Manufacturing Technology) at Chalmers University of Technology from August 2013 until August 2018. Part of the activities in paper E were carried out at DTU Risø in Denmark. The project is done under the supervision of Professor Johan Ahlström and co-supervision of Professors Magnus Ekh and Christer Persson.

Thesis

This thesis consists of an extended summary and the following appended papers:

Paper A D. Nikas, J. Ahlström, and A. Malakizadi. Mechanical properties and fatigue behaviour of railway wheel steels as influenced by mechanical and thermal loadings. *Wear* **366-367** (2016), 407–415. ISSN: 00431648. DOI: 10.1016/j.wear.2016.04.009

Paper B D. Nikas and J. Ahlström. Characterization of microstructural changes in near pearlitic steels using orientation imaging microscopy - Influence of predeformation on local sensitivity to thermal degradation. *IOP Conference Series: Materials Science and Engineering* **89**.1 (2015), 6–12. ISSN: 1757899X. DOI: 10.1088/1757-899X/89/1/012039

Paper C K. A. Meyer, D. Nikas, and J. Ahlström. Microstructure and mechanical properties of the running band in a pearlitic rail steel: Comparison between biaxially deformed steel and field samples. *Wear* **396-397**.August 2017 (2018), 12–21. ISSN: 00431648. DOI: 10.1016/j.wear.2017.11.003

Paper D D. Nikas, X. Zhang, and J. Ahlström. Evaluation of local strength via microstructural quantification in a pearlitic rail steel deformed by simultaneous compression and torsion. *Under review for international publication* (2018)

Paper E D. Nikas and J. Ahlström. High temperature uniaxial ratcheting and bi-axial low cycle fatigue behaviour of railway wheel steel. *To be submitted for international publication* (2018)

Papers A-E were prepared in collaboration with the co-authors. The author of this thesis was responsible for the major progress of the work, i.e. took part in planning the papers, carried out the experiments, analysed the results and wrote the main part of the papers. Experimental work for Paper D was done in collaboration with the second co-author in Denmark and results processing was done with his help.

Papers not appended to the thesis:

(i) D. Nikas and J. Ahlström. "Thermal deterioration of railway wheel steels". *Proceedings of the 35th Risø International symposium, Risø, Denmark, p. 411-420.* 2014

(ii) A. Esmaeili et al. "High Temperature Tread Braking Simulations Employing Advanced Modelling of Wheel Materials". *Proceedings of the 11th International Heavy Haul Association conference, Perth, Australia.* 2015

(iii) D. Nikas, K. A. Meyer, and J. Ahlström. Characterization of deformed pearlitic rail steel. *IOP Conference Series: Materials Science and Engineering* **219**.1 (2017). ISSN: 1757899X. DOI: 10.1088/1757-899X/219/1/012035

Contents

Part I
Extended Summary

1 Introduction

1.1 Motivation

One of the most important aspects in railway operation is the interaction between rail and wheel. If one takes into account that each railway wheel is loaded with a static weight of up to 12.5 tonnes, and that the contact patch between these two components is around the size of a small coin, it is clear that very high loads act on a very small area, that in combination with other factors, give rise to wear and damage in both components. Frictional forces on the surface of wheels and rails caused by recurring acceleration, braking, curving and occasional slippage can cause cyclic plastic deformation and heating, which in turn causes an aligned, anisotropic microstructure with altered mechanical behaviour. Control of material property degradation is an important topic for guiding maintenance, as well as ensuring safety of railways, since it will allow for a more accurate prediction of material wear and lifetime. The railway industry still relies on steels for the manufacturing of wheels and rails. Carbon steels or low alloy steels with a mostly pearlitic microstructure are the dominating materials for these applications, due to their combination of high strength and good wear properties in relation to cost. Heat treatment procedures can give wheel materials a near pearlitic microstructure with finer pearlite closer to the wheel tread surface and favorable residual stress distribution. Rails are typically made from steels with slightly higher carbon content, heat treated to a fully pearlitic microstructure. Bainitic microstructures have been tried out for both wheel and rails and put into service, but still the pearlitic grades strongly dominate the market. It is of critical importance to study the material microstructure and understand how it performs under a complex combination of mechanical and thermal loadings and how this microstructure is affected by all the various factors that come into play in service. Understanding how railway materials behave is essential for materials selection for different environments, design of railway components, as well as tuning of traction and braking systems.

1.2 Aim and scope of research

This thesis focuses on the deterioration of microstructure and mechanical properties of railway wheel and rail steels after exposure to high temperatures and plastic deformation. Specifically examined, were the medium carbon wheel steels UIC ER7T and ER8T ($\sim$0.55 wt.% C) and rail steel R260. During their service life, the surface layers of rails and wheels are subjected to very high rolling contact loads. These lead to accumulation of large shear strains close to the running surface (see e.g. [1, 2]). Moreover the high thermal loads, especially for wheels, can cause severe degradation of the material microstructure, more

specifically, spheroidisation of the pearlite, which combined with plastic deformation (that makes the material more prone to spheroidisation) can lead to severe deterioration of the material's mechanical properties. The sensitivity towards degradation processes and crack formation is dependent on material chemical composition and starting microstructure.

The aim of this work is to help judging limits for utilisation of wheel and rail materials, with respect to combined cyclic mechanical and thermal loadings. The focus in this project was to quantify the changes in mechanical performance of pearlitic and near-pearlitic railway steels exposed to both separate and combined mechanical and thermal loadings up to 650°C.

Since railway wheels are exposed to block braking in freight trains operation, high temperatures are evolving, so relevant testing conditions are necessary to understand their behaviour. This was done by first investigating the changes in room temperature hardness, that are induced by thermal degradation with and without prior plastic deformation. A microstructural evaluation was made to correlate results from hardness testing with the microstructural degradation, and to examine microstructure variations with depth below the running surface. The elevated temperature performance was studied by uniaxial low cycle fatigue experiments followed by axial-torsional fatigue experiments. Both were performed at high temperatures and results were correlated afterwards. The study complements the literature about mechanical behaviour of near-pearlitic wheel steels exposed to combined thermal and mechanical loadings and provides a better understanding and quantification of how the material properties will vary with depth below the wheel tread; an important issue since material at larger depth becomes exposed to surface loadings after wheel reprofiling during maintenance. EBSD was used in an attempt to evaluate the influence of orientation gradients (according to literature correlating with the dislocation density) on the degradation of microstructure, and to examine how it changes with increasing heat treatment temperature.

For the rail material, a predeformation method to replicate the microstructure that is found in the surface layer of rails was developed in another Charmec project [3] and the studies presented in this thesis are focused on evaluating how well this artificially created microstructure corresponds to the one seen in samples retrieved from the field. Then an effort to fully characterise this microstructure was made by correlating dislocation density in the material with various shear strain levels that are produced with the above mentioned predeformation method.

2 Background

2.1 Railway operation conditions

Axle loads for passenger trains in Europe vary between 15-25 tonnes [4] and can go even higher when it comes to freight trains. A typical wheelset that should carry this load is shown in Fig. 2.1. The contact patch for a standard profile rail and wheel (and 11 tonnes contact force) is elliptical with 18 x 11 mm for the major and minor axis of the ellipse [4]. If the wheel is worn, the shape becomes more circular due to the wheel profile becoming more conformal and thus a small change in lateral position with respect to the rail occurs. When the dynamic effects and tractive forces are added, it becomes evident that very high demands are put on the materials selected for these components. Moreover, higher speed and load demands from the railway industry increase the requirements on the material quality of wheels and rails. Another important aspect of railway operation is regular maintenance. The service life of a wheel can vary between 300.000 and 2.500.000 km and during this lifetime, two to five reprofilings are necessary to remove surface defects and cracks that might have appeared. This procedure exposes new material on the surface of the wheel that has slightly different properties than the original surface [4]. Control of material property degradation in wheels is an important topic for guiding maintenance, to minimise life cycle cost and ensuring safety of railways.

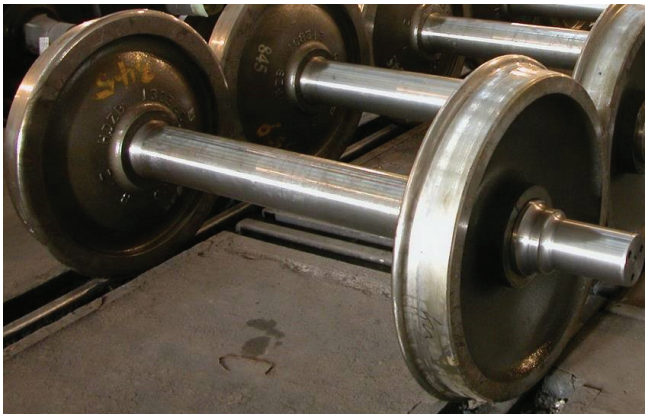

Figure 2.1: *A typical wheelset*

The areas of the wheel that are affected the most during operation are the flange, the flange root and the tread and for the rail the running surface, gauge corner and gauge face, see figure 2.2.

Wear is the main issue for the flange and the flange root but for the tread, in addition to wear, there is also crack development that is often denoted rolling contact fatigue (RCF) and thermal loading coming from frictional heating. Frictional forces arise in the wheel-rail contact and in the case of block braking, also in the contact between block and wheel. In practice temperatures over 500°C can be achieved [5] during pronounced block braking. Even higher temperatures up to approximately 1050°C can be reached on occasional slippage when the wheels skid along the rail for a short time [6, 7]. This

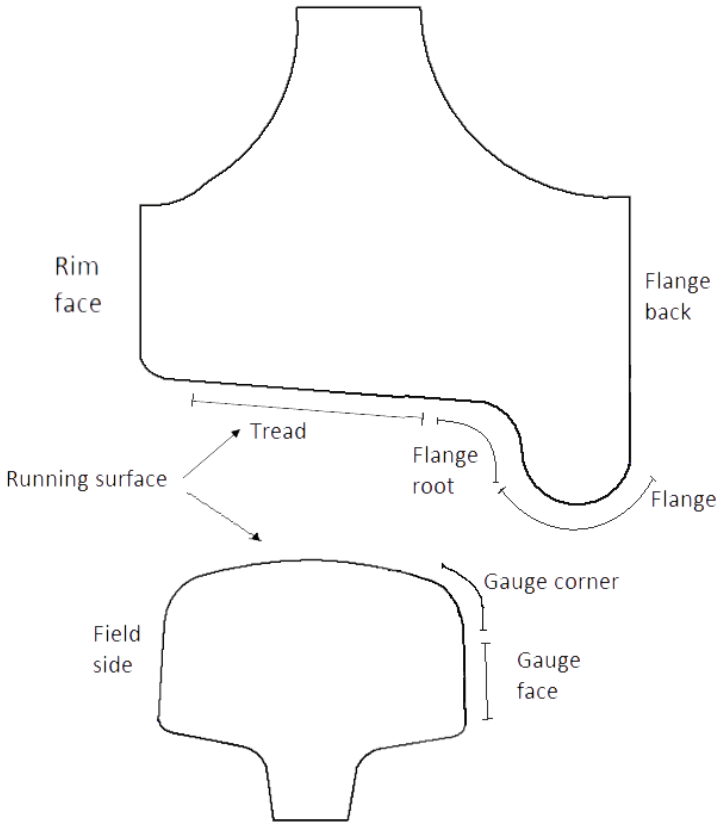

Figure 2.2: *Typical geometry and nomenclature of parts of the wheel rim and rail head*

causes phase transformation to austenite in the steel, often resulting in brittle martensitic patches on the wheel tread that can lead to spalling and other problems. Due to the volume change from this phase transformation residual compressive and tensile stresses are induced in the material that make it prone to cracking when additional load is applied [8]. Although traction control systems in passenger trains have improved during recent years, reducing thermal events, on freight trains that still operate on simpler designs and carry higher axle loads, these phenomena are present to a higher extent. These high temperature phenomena up to 700°C often cause microstructural changes that cause the mechanical properties of the material to deteriorate significantly. In the outermost millimeters of the wheel tread, the material also experiences large deformation and plastic flow due to creepage. This makes it even more prone to spheroidisation [9].

For the rails, large shear strains close to the running surface and alignment of microstructure due to deformation are the main causes of crack initiation. Rolling Contact Fatigue (RCF) is also present and is one of the main sources for maintenance costs for the railway industry [10, 11].

The following sections in this chapter will describe the microstructural related phenomena that occur in wheel and rail material when exposed to high temperatures and mechanical loads.

2.2 Materials for railway wheels

The most common wheel materials used for rolling stock today are carbon steels with around 0.5 wt% carbon, heat treated to give a near-pearlitic microstructure close to the tread surface. Different standards and steel designations exist around the world, shown on table 2.1 [12, 13].

Table 2.1: Wheel materials used for rolling stock

Specification	**Steel grade**	**Carbon content(%)**
EN13262	ER6	≤ 0.48
	ER7	≤ 0.52
	ER8	≤ 0.56
	ER9	≤ 0.60
AAR M-107/M-208	Class L	≤ 0.47
	Class A	0.47-0.57
	Class B	0.57-0.67
	Class C	0.67-0.77
	Class D	
JIS E 5402-1	SSW QS	0.60-0.75
	SSW QR	
	SSW QRH	

There are two grades that are mostly used on trains in Europe; the ER7 grade is the dominating grade on freight trains and on many passenger coaches using block braking, while the ER8 grade with slightly higher carbon content is often used for passenger trains with driven wheels, so called EMUs (Electric multiple units) [14]. In production, after forging and rolling, wheels are rim chilled; a heat treatment yielding a microstructure consisting of fine pearlite with some 5-10 vol.% pro-eutectoid ferrite just below the wheel tread [15]. After this heat treatment the letter "T" is added to the designation, so in this thesis the commonly used names R7T and R8T will be used.

2.3 Materials for rails

The most common rail materials used are medium and high carbon steels heat treated to give a fully pearlitic microstructure without or with forced cooling of the rail head, "head hardening". Besides carbon content, the rail grades are usually also specified depending on their hardness level. Some bainitic grades are also available for use in specific situations. Different standards and rail steel designations exist around the world, shown on table 2.2 [16, 17].

The grades with the lower carbon contents are used for normal track and the higher alloyed and heat treated grades are used in switches, crossings and curves since more severe conditions are encountered in the latter cases [18].

Table 2.2: Rail materials

Specification	Steel grade	Carbon content(%)	Hardness (BHN)	Description
EN 13674-1	R200	0.40-0.60	200-240	Non-heat treated
	R220	0.50-0.60	220-260	Non-heat treated
	R260	0.62-0.80	260-300	Non-heat treated
	R260Mn	0.55-0.75	260-300	Non-heat treated
	R350HT	0.72-0.80	350-390	Heat treated
	R400HT	0.90–1.05	400-440	Heat treated
UIC 860-O	700	0.40-0.60		
	900A	0.60-0.80		
	900B	0.55-0.75		
	1100	0.60-0.82		

2.4 Morphology and formation of pearlite

Pearlite is a two-phase structure formed during diffusional transformation from Fe-C austenite, with a chemical composition of Fe ∼0.77 wt% C. It grows from a number of nuclei that exist in the austenite grain boundaries [19]. These nodules grow until they finally meet with each other. The nodules are built from pearlite colonies consisting of alternating lamellae of ferrite (Fe) and cementite (Fe_3C) with a single orientation (Fig. 2.3). In steels with similar hypo-eutectoid composition (lower C content), free ferrite formed before the eutectoid pearlite formation, thus called "pro-eutectoid ferrite" is also present in the microstructure.

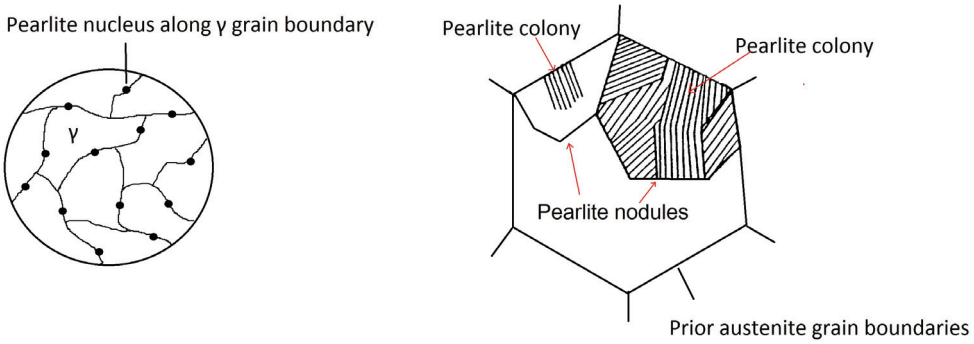

Figure 2.3: *Sketch of pearlite formation*

The transformation temperature determines the resulting interlamellar spacing, controlled by the carbon diffusion rate. Thus, it can be manipulated using specific heat treatments depending on the chemical composition of the material. Heat treatments that employ rapid cooling have the ability to delay the transformation temperature to lower temperatures, which in turn results in larger volume fraction of pearlite (with slightly

hypo-eutectoid composition) and a refined lamellar structure [20]. The nodule size is affected by the prior austenite grain size but has little effect on interlamellar spacing [21]. It was also shown that colonies within the same nodule have a similar interlamellar spacing [22].

2.5 Dislocation motion theory

Deformation in crystalline solids occurs with the generation, movement and accumulation of dislocations under an externally applied stress. Dislocation movement is limited by internal stress fields from different kinds of obstacles. The mobility of dislocations thus depends on thermally activated processes like by cross-slip and climb that enable dislocations to circumvent the obstacles [23]. The velocity with which they move depends on the rate they are able to overcome these obstacles [24]. For pure metals, the main obstacles are stress fields from other dislocations, but for alloys where atoms of different elements are in solid solution, there are significant contributions from other sources as well [25]. The level of thermal activation that is necessary to overcome an obstacle is different depending on the kind of obstacle, since these can have different strength or spacing between them [26]. Two regions exist for the dependence of the dislocation velocity with respect to stress and temperature. The first concerns low velocities and follows an Arrhenius-type behaviour, i.e. it increases with temperature and the second concerns higher velocities where the temperature dependence is reversed. Only in the first region, dislocation motion is thermally activated [25, 27].

2.6 Strength of pearlite

Increasing the carbon content increases the steel's strength, often at the expense of fracture toughness. More specifically, for steels near the eutectoid composition with some free ferrite present, the interlamellar spacing is associated with controlling strength, whereas the ferrite phase governs ductility [28]. Refinement of the interlamellar spacing limits the dislocation movement, which mainly occurs in the ferrite lamellae, and effectively increases the steels' strength. Refinement can be accomplished by lowering the transformation temperature (by controlling the cooling rate). The strength of pearlite follows a Hall-Petch type relationship:

$$\sigma_y = \sigma_0 + \kappa_y S^{-\frac{1}{2}} \tag{2.1}$$

where S denotes the interlamellar spacing and σ_y is the yield stress. The material constants σ_0 and κ_y are used for the necessary stress for dislocation movement in the ferrite (also called friction stress) and the strengthening coefficient (or dislocation locking) respectively [15, 29, 30]. The yield strength of pearlite is mainly dependent on the interlamellar spacing and is independent of prior austenite grain size or nodule diameter [28].

The fact that the interlamellar spacing decreases as transformation temperature decreases is more pronounced with increasing carbon content. Also the less the carbon

content of pearlite, the larger the interlamellar spacing according to Bae et al. [31]. It was found that the carbon content is more influential than interlamellar spacing or prior austenite grain size, when it comes to ductility.

When it comes to hypo-eutectoid steels, it was reported [32] that the strength of pearlitic colonies did not follow a Hall-Petch type relationship based on interlamellar spacing and varied even though the interlamellar spacing was kept constant. This was attributed to the influence of hydrostatic stresses due to the presence of the free ferrite phase; the difference in thermal expansion causes stresses of opposite nature in the two phase constituents of the microstructure (compressive hydrostatic stresses in the ferrite and tensile in the pearlite).

A very important consideration when it comes to pearlitic steels is how the lamellar microstructure interacts with the dislocations when the material is subjected to external loadings, either monotonic or cyclic. The density of dislocations that are produced during cyclic loading is much higher than the amount that is produced at monotonic loading for similar stress levels. Moreover, during a monotonic test reaching larger strains, slip planes are rotating towards the tensile axis, which is not the case for fully reversed cyclic loading [33]. According to the model proposed by Miller-Smith [34] dislocations pile up on the interface between cementite and ferrite. Stress concentration eventually leads to the fracture of the cementite lamellae and plastic deformation continues in the neighbouring ferrite lamellae. Strain localisation happens only on a few glide planes.

Based on the above assumption that dislocation sources exist on the interface between cementite and ferrite in a local micro yield region, the yield strength of pearlite depends on the necessary stress to move dislocations in ferrite between two cementite walls, thus it increases with the refinement of the interlamellar spacing which in turn leads to strengthening of the material [35].

2.7 Pearlite spheroidisation

At exposure to temperatures approaching the $\alpha - \gamma$ transformation line (A_{C1}), an increasing microstructural degradation occurs. According to common heat treatment practice, depicted within a binary iron-carbon phase diagram (Fig 2.4), there exists a distinct zone where spheroidisation occurs. Initially the pearlite lamellae start to break up and then coarsen until we get closer to A_{C1}, where cementite lamellae turn into spheroids (Fig 2.5). Exposure to high temperatures for longer times is known to cause softening of the material [15]. It was also found that longer time durations cause more pronounced spheroidisation [36].

As the pearlitic lamellar structure is never perfect in reality, there are always morphological growth faults, that exist such as holes, kinks, striations, etc. Previous studies have shown that break-up of the lamellae during static annealing happens at regions of such growth faults that were generated during the initial formation of the pearlite. Spheroidisation can also initiate from these faults and expansion of such holes and thickening of the lamellae occurs [38, 39]. This continuous growth leads to break-up of large cementite platelets into small particles and then these small particles evolve into spheroids. The driving force is the chemical potential gradient between faults with various shapes and

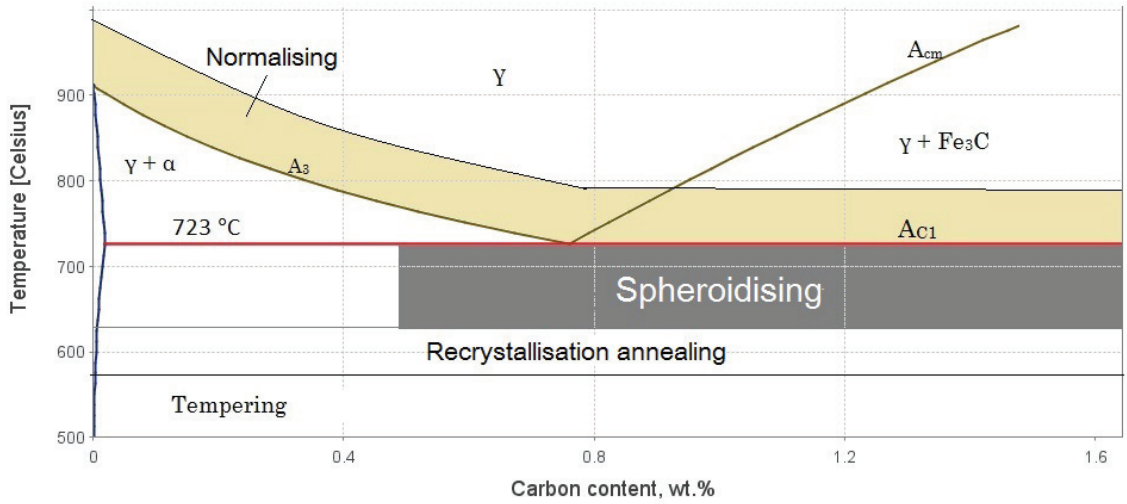

Figure 2.4: *Phase diagram of the iron-carbon system (up to 1.6 wt.% C) calculated using Thermo-Calc with fields indicating typical heat treatment temperatures re-drawn from ASM handbook [37]*

the neighbouring interfaces. In a 2D image the onset of spheroidisation appears as a coarsening in the lamellar thickness [39].

Moreover, with the addition of cold work, cementite lamellae break and step bands are created in some of the pearlite colonies that can initiate spheroidisation. In cases of hot deformation, preferential break-up sites are created by dislocation structures and are believed to accelerate spheroidisation by providing short circuit paths for diffusion. In addition, extra vacancies are being generated, because of the deformation that increase diffusion rates of carbon and iron [9].

For temperatures far below the $\alpha - \gamma$ transformation line (A_{C1}), damage appears more slowly.

Given the above theoretical background, an attempt to connect this to railway wheel material degradation was made. Previous investigations combining low cycle fatigue loading and elevated temperatures have shown a cyclic hardening at 300°C and cyclic softening at higher temperatures for virgin material ER7 [40, 41]. The change in room temperature (RT) hardness after exposure to elevated temperatures between 500°C up to 725°C was also studied before for the ER8 grade [15]. It was also shown that the two grades, ER7T and ER8T, behave similarly under cyclic loading with respect to hardening and softening and only differ in stress levels due to the slight difference in carbon content.

2.8 Strain ageing and Dynamic strain ageing

Strain ageing in metals refers to the time dependent phenomenon of impeding dislocation motion by segregation of mobile solute atoms. By diffusing to positions around dislocations where atoms find a low energy position, and thus decrease the local stress level, these

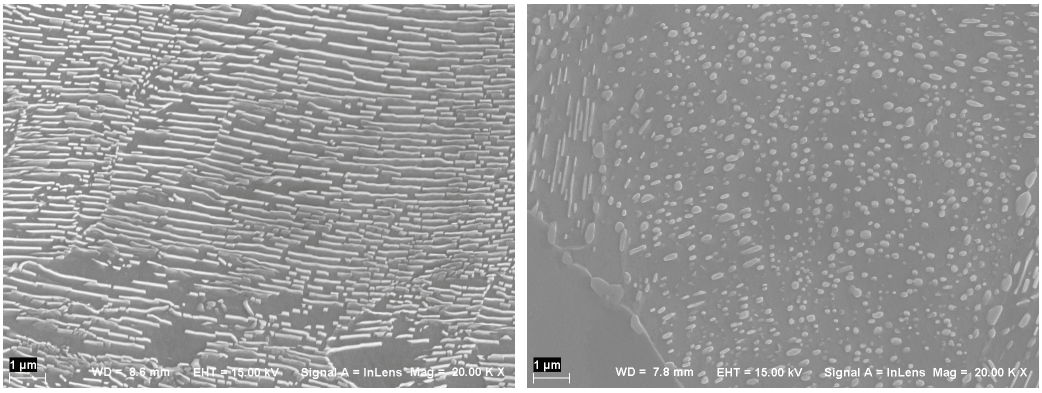

(a) (b)

Figure 2.5: *Scanning electron micrographs of pearlite microstructure after heat treatment. (a) Initial lamella break up, and (b) complete spheroidisation.*

have the ability to temporarily arrest dislocations [42]. According to Cottrell-Bilby theory [43] it is a two-step process, with the first step being the rearrangement of interstitials and formation of solute atmosphere around dislocations and the second is the formation of discrete clusters or precipitates [44]. In iron based alloys and more specifically, carbon steels, this phenomenon is associated with interstitially dissolved atoms of carbon and nitrogen during deformation [45]. There are two types of strain ageing; static strain ageing and dynamic strain ageing. Static strain ageing refers to the increase in yield stress that is observed in alloys when a specimen is strained to a certain level, then unloaded fully or partially and aged for a specific amount of time. After the ageing treatment, if strained to the same level as before, an increase in tensile strength will be observed. Further, in steels, static strain ageing causes the appearance of an upper and lower yield point and decreases the total elongation of the material [44].

In dynamic strain ageing (DSA), the dislocations are pinned at obstacles repeatedly during the straining process at high temperature, for example, during a cyclic test at high temperature [46] or during a monotonic test. During such a test dislocations surmount obstacles with the combined help of stress and thermal activation. Dislocations segments are arrested for a certain amount of time until they overcome the obstacle and then go to the next one with a higher velocity. The movement of solute and interstitial atoms by diffusion to the dislocations during this waiting time is called dynamic strain ageing or Portevin-Le Chatelier effect (PLC) [47]. This gives a serrated flow stress curve, seen in a tensile test with a suitable combination of temperature and strain rate. DSA is responsible for the increased hardening that is observed during a cyclic fatigue test within a parameter window, where strain rates and temperatures are producing this effect for the specific material and condition. So for both static and dynamic strain ageing, the evolution of dislocation density has a large influence on the strain ageing process [46].

2.9 Dynamic strain ageing in low cycle fatigue tests

Fatigue life for a given stress amplitude and mean stress typically decreases with increasing temperature [48]. When a material is subjected to a low cycle fatigue (LCF) experiment at an elevated temperature and at a low frequency, time-dependent processes such as creep, oxidation and dynamic strain ageing influence its mechanical behaviour (stress response including cyclic hardening) and fatigue life [49]. Dynamic strain ageing shows during a LCF test as serrations, sudden load drops, jerkiness or other discontinuities in the stress strain curve that gives it the 'staircase' type appearance. Serrated flow in cyclic tests can occur at lower temperatures than under monotonic deformation tests since non-equilibrium vacancies and dislocations that are generated during fatigue deformation enhance the diffusion of solute atoms. Another consequence of serrated flow is that it promotes localisation of plastic flow, that in some cases leads to reduced fatigue life [50]. Dynamic strain ageing (DSA) is thus responsible for the increased hardening that is observed during a cyclic low cycle fatigue test within the current parameter window. Both the hardening within one specific loop, and the cyclic hardening (or softening) occurring throughout the fatigue life can be affected by DSA. So, apart from the serrated flow, the main effect of dynamic strain ageing during low cycle fatigue testing reported in literature, is the increased cyclic hardening in a temperature range of 250-400°C [45, 49].

2.10 Orientation gradients and dislocation density in pearlite

While interlamellar spacing, prior austenite grain size and other morphological features are important when evaluating the strength of pearlite and the sensitivity of the material to spheroidisation there are other microstructural factors that can affect it, such as dislocation density or the elements in solid solution. Local misorientations in the microstructure is another factor that can affect the spheroidisation behaviour of the material. These are the result of a combination of the elastic strain field, but more importantly, they originate from the curvature of the crystal lattice that is associated with geometrically necessary dislocation density [51]. It was found that pearlitic ferrite (and presumably the cementite) contains a lot of orientation gradients (in contrast to the pro-eutectoid ferrite), that suggests there is a certain density of geometrically necessary dislocations present [52]. It was concluded that in order to fully understand the mechanical properties of pearlite, the dislocation density of the pearlitic microstructure needs to be taken into account. With this in mind the heat treated wheel material was evaluated using EBSD technique as it is associated with estimating dislocation density and distribution in a material, as well as strain fields that exist in the material microstructure [53, 54].

3 Experimental procedures

3.1 Materials

The steels studied in the present work were the ER8 and ER7 wheel steel grades and the R260 rail grade. These materials follow the standards EN 13262-1 [12] and EN 13674-1 [17]. The actual chemical composition of the materials studied is shown in Table 3.1.

Table 3.1: Chemical composition of materials studied, in wt%

	C	Si	Mn	Mo	S	Cr	Cu	Ni	V	P	Al	N	Fe
R7T	0.50	0.36	0.80	0.03	0.002	0.2	0.15	0.12	0.023	0.008	-	-	Bal.
R8T	0.59	0.35	0.78	0.05	0.006	0.13	-	0.17	<0.005	0.005	-	-	Bal.
R260	0.72	0.31	1.04	-	0.010	0.02	0.018	-	<0.005	0.006	<0.002	0.006	Bal

The rim chilling heat treatment (the wheel tread and flange are cooled with water jets after austenitisation) that the wheel materials undergo during production, creates a fine-pearlitic microstructure close to the rim with a slight decrease in hardness and strength and a slight increase in free ferrite and interlamellar spacing with increasing depth. The rail material has no additional heat treatment after its manufacturing that includes rolling and subsequent cooling.

The initial microstructures of these materials are shown in figure 3.1. The two wheel steels have a similar composition with only a slight difference in carbon content. Hence their microstructure looks almost identical. The initial microstructure consists of pearlite (dark areas in figure 3.1a-d) and some pro-eutectoid ferrite (appearing bright in figure 3.1a-d). The difference in carbon content leads to R7T having higher free ferrite content than the R8T. Typical interlamellar spacing of the pearlite is around 130 nm and hardness around 270 HV for material closer to the wheel tread. These values change slightly as we move deeper into the wheel away from the running surface. The rail material (figure 3.1c-d) has a fully pearlitic microstructure with interlamellar spacing of around 230 nm and hardness of 290 HV.

The following investigations were done with the different materials.

3.2 Microstructural degradation of R8T wheel material (Papers A and B)

Change in room temperature (RT) hardness of R8T wheel material after exposure to elevated temperatures of 250 to 650°C was examined in the following conditions:

1. Undeformed (taken from an un-used wheel, “virgin material”).
2. After monotonic pre-straining to 6.5 % plastic strain.

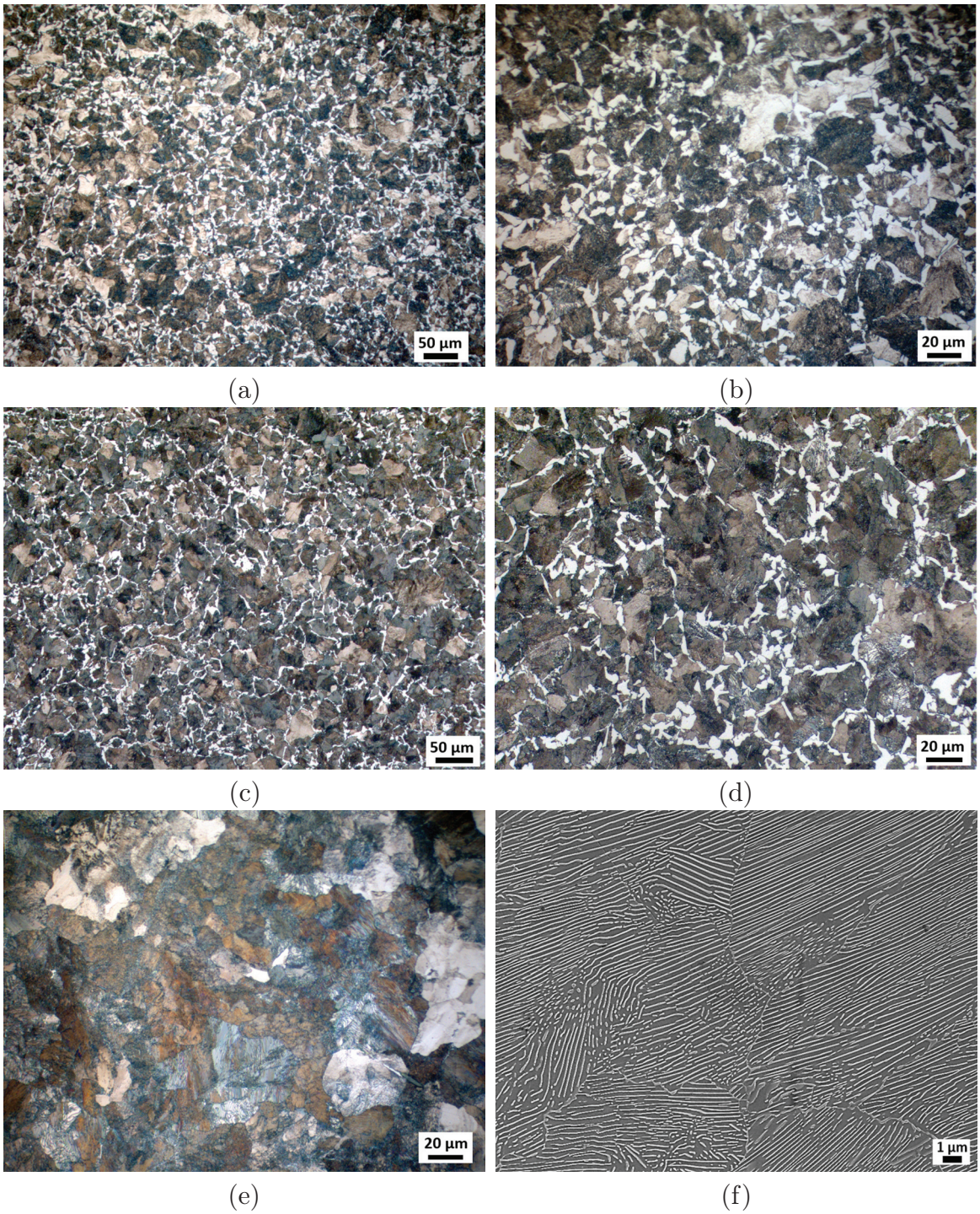

Figure 3.1: *Micrographs of the three materials(a) R7T low magnification (b) R7T high magnification (c) R8T low magnification (d) R8T high magnification (e) R260 high magnification and (f) R260 SEM image, very high magnification*

3. After cyclic pre-straining at $\Delta\epsilon_t/2 = 1.0$ % until saturation.

The degradation of the microstructure at high temperature was in focus and correlated to the hardness change measured. Material at greater depths below the wheel tread surface experiences slower cooling in production, which gives a decreasing hardness with depth. To extend the validity of the results for a wider range of heat treatments, or depth below the surface, hardness at increasing depth below the surface was measured and correlated with microstructural parameters examined by scanning electron microscopy and optical microscopy. Specifically, the ferrite content and lamellar spacing was measured at different depths (paper A). The second component of this study was to examine R8T wheel material using EBSD technique for samples with different heat treatments and different pre-strain conditions (paper B).

Tensile bars with thickness 5 mm and "dog bone" shape were taken from a virgin R8T wheel at a depth of around 20 mm below the running surface. These bars were pre-strained using an Instron electro-mechanic tensile machine to 6.5 % longitudinal strain. Two extensometers were used to prove an even strain distribution. Tests were run in strain control at a strain rate of $10^{-4}s^{-1}$. Samples were taken from the waist of the pre-strained bars and cut into pieces around $5 \times 8 \times 8\ mm$, to be used for hardness testing and heat treatment experiments. Similar pieces were taken out from cylindrical specimens from a depth of 15 mm below the running surface that had previously been exposed to uniaxial push-pull low cycle fatigue experiments at room temperature; constant strain amplitude loading at $\Delta\varepsilon_t/2 = 1.0\%$ run until failure (approximately 1300 cycles). All specimens were ground and polished down to 1 μm diamond suspension before the hardness measurements and heat treatments.

Vickers hardness measurements were performed in undeformed and pre-strained R8T materials before heat treatment, using an applied load of 10 kg in a Wolpert 2RC hardness tester. Then the samples were put in a tube furnace with a nitrogen inert atmosphere to prevent oxidation and decarburisation. Both undeformed and pre-strained samples were heat treated for 4, 28 and 238 minutes at various temperatures in the range 250°C-650°C. After heat treatments at selected times and temperatures, new room temperature hardness measurements were performed, again with a 10 kg load. For both measurement series, indentations were placed randomly on the specimen surface at a distance more than twice the diagonal length from the previous indentation. The hardness was taken as the mean value of three indentations that were measured with an optical microscope afterwards to decrease the error in reading.

3.3 Microstructural investigation of R8T wheel material (Paper B and unpublished)

The R8T wheel steel was studied with light optical microscopy (OM) and scanning electron microscopy (SEM), to evaluate the microstructure. Electron backscatter diffraction (EBSD) technique was also employed, to evaluate the orientation gradients in the initial and as-heat treated condition. The specimens were mechanically ground and polished to 0.04 μm using a colloidal silica suspension. Etching was done using Nital (3 % HNO3 in

ethanol) to gain some topographical contrast and thus be able to map regions of interest. The high resolution micrographs and the EBSD measurements were carried out in a LEO 1550 high resolution field emission scanning electron microscope (FEG-SEM). The system was equipped with an EBSD detector (Nordlys, Oxford instruments), a high speed camera for EBSD pattern recording and software for crystal orientation mapping (AztecHKL). The samples were tilted to have their normal 70° to the incident beam and the SEM was operating at an accelerating voltage of 20 kV. Crystallographic orientation maps were taken on the pearlite colonies as well as on the pro-eutectoid ferrite with a step size of 130 nm which is around the interlamellar spacing of the pearlite in this material. The EBSD patterns of the pearlitic cementite were of insufficient quality and were thus omitted from the analysis.

Using a large number of SEM images of R8T wheel material and processing them with Matlab, image analysis was performed to quantify the amount of pearlite spheroidisation at the various temperatures examined. For this analysis, 150 SEM images per sample were taken. The first step in the analysis is the segmentation; to determine what is cementite and what is ferrite. First, a median filter was applied to the image. This was done to reduce the salt-and-pepper noise of the image. Then the contrast of the image was improved, using one of Matlab's built in- functions (imadjust).The image can now be made binary where the levels 0 and 1 correspond to black and white. To disconnect regions connected with just a few pixels, an opening filter was applied. Very small regions (fewer than 10 pixels) were then removed. Possible holes in the white regions were also filled.

A theoretical value of cementite was calculated using the lever rule [55]:

$$V = \frac{C_0 - C_a}{C_{Fe_3C} - C_a} \tag{3.1}$$

where C_{Fe_3C} is the content of carbon of the cementite (6.67 wt.% C), Ca is the carbon content of ferrite (0.02 wt.% C) and C0 is the carbon content of the R8T wheel steel of our investigation. So the expected volume fraction of cementite is 8.1 % in this case. Due to several reasons, one being the observed angle of the pearlitic plates, the cementite area will be overestimated in the images most of the time. To deal partly with this problem, the cementite regions were "thinned" using the respective matlab function. The result of each step is visualised in figure 3.2.

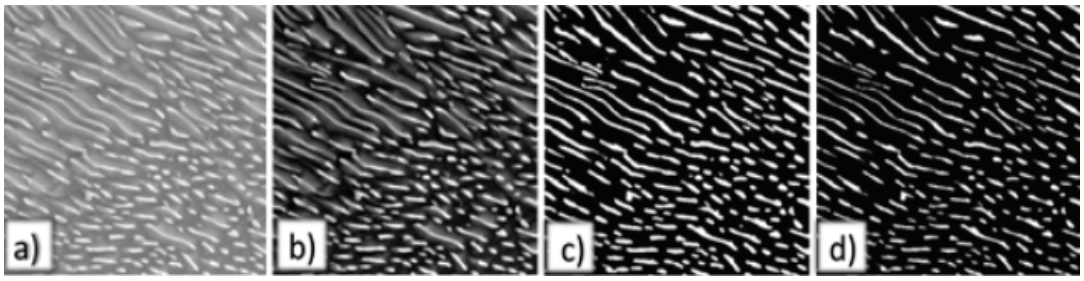

Figure 3.2: *Image processing example: a) original image b) Noise removal and contrast enhancement c) Image made binary d) Final image obtained as described in text*

To discriminate lamellar from globular regions, one has to define simple rules and

characterise the regions individually. Chattopadhyay and Sellars [56] propose that the discrimination should be based on the length over width ratio of the regions; Regions should be considered as globular if the length over width ratio is lower than 8. To be able to separate lamellae from spheroids with this criterion, the length and width of every region has to be measured. According to Nutal [57], the most efficient and accurate way to generalise the shape of a region is to assume the shape as ribbon-like. Following this method, the length (L) and width (W) of each region can be estimated using:

$$L = \frac{1}{2}\left(\frac{P}{2} + \sqrt{\left(\frac{P}{2}\right)^2 - 4A}\right) \text{ and } W = \frac{1}{2}\left(\frac{P}{2} - \sqrt{\left(\frac{P}{2}\right)^2 - 4A}\right) \tag{3.2}$$

where P and A are the perimeter and area of each region. First calculated in pixels and then converted to actual distance using the scale bar that exists on every SEM image. Using this method, the length over width ratio could be calculated and the regions could be characterised as lamellar or globular (figure 3.3).

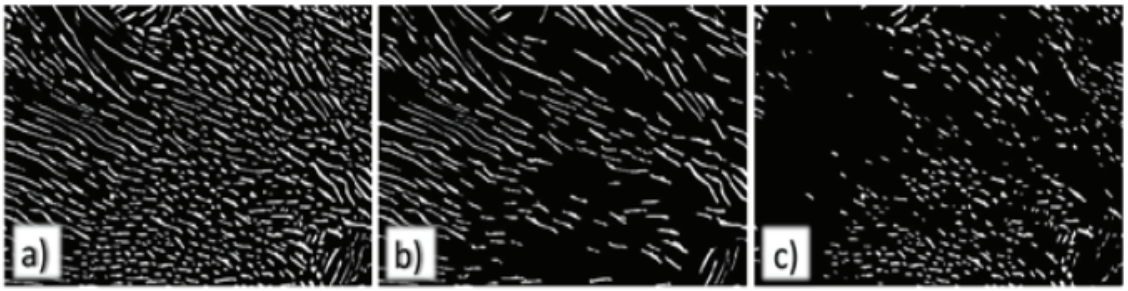

Figure 3.3: *Image discrimination: a) Segmented image obtained as described in text, all regions included b) Lamellar regions c) Globular regions*

Using the above method the total percentage of cementite and both quantities of globular and lamellar cementite can be calculated.

3.4 Elevated temperature behaviour of R7T wheel material (Papers A and E)

An attempt was made to complement the picture from literature of mechanical behaviour of R7T wheel material exposed to cyclic plastic deformation at elevated temperatures. This was accomplished by:

1. Uniaxial strain-controlled low cycle fatigue (LCF) behaviour at elevated temperatures 250°C-600°C and including hold times during which stress relaxation could be studied (paper A).

2. Load controlled ratcheting experiments with mean stress included at elevated temperatures 200°C-500°C (paper E).

3. Biaxial strain-controlled low cycle fatigue behaviour at elevated temperatures 200°C-400°C (paper E).

All tests were performed on material from virgin wheels of the R7T material and samples were taken out from the wheel rims parallel to the running direction, at a depth of approximately 15-20 mm below the running surface.

For the uniaxial LCF tests, cylindrical test bars with gauge diameter 6 mm were produced and ground to 800 grit. Low cycle fatigue tests were run in an Instron servo-hydraulic test frame in strain control. Tests were run at constant total strain amplitude $\Delta\varepsilon_t/2$ of 0.6 % with triangular wave shape at $R_\epsilon = -1$ and strain rate $5 \times 10^{-3} s^{-1}$ giving a cycle time of 4.8 s. (Tests with $\Delta\varepsilon_t/2 = 0.4$ % and $\Delta\varepsilon_t/2 = 1.0$ % were also run under the same conditions, but are not focused on in this thesis). Peak/trough values were recorded for every cycle, and full hysteresis loops were recorded for the initial 25 cycles and thereafter regularly during the whole lifetime. Several tests were run with hold periods repeating every 500 cycles. These hold periods had a duration of 30 min, and the stress relaxation under constant compressive strain of -0.6 % was recorded. The test durations varied between 4 and 8 h depending on temperature. The machine was equipped with a furnace to perform isothermal tests at elevated temperatures from 250°C to 600°C without atmosphere control. Specimens were first mounted in the grips, the furnace was sealed with insulation wool and heated until the temperature of the specimen became stable at the desired level. All tests were run under constant temperature until failure.

Similar bars were also used for the ratcheting experiments. These were run with a mean stress and stress amplitude of 100 ± 500 MPa at elevated temperatures of 200°C, 300°C, 400°C and 500°C. The hold times were replaced in these tests for 15 faster cycles that were run at a rate of 5 Hz, with 85 cycles run at 0.5 Hz in between. The reason for limiting the number of rapid cycles is to avoid excessive heating. Due to the loops being unclosed in each cycle the ratcheting strain ε is defined as the average maximum and minimum strain in each cycle as in:

$$\varepsilon = \frac{1}{2}(\varepsilon_{max} + \varepsilon_{min}) \tag{3.3}$$

Lastly, for the biaxial experiments that were done, test bars were taken 20 mm below the running surface as shown in figure 3.4. These bars were then turned between centers into cylindrical bars to the desired dimensions and thereafter drilled to create thin-walled fatigue test bars. The bars were larger in dimensions than the previously used ones, with 14 mm outer gauge section diameter and 12 mm inner. Care was taken during the machining process to achieve a very smooth inner and outer surface, so that minimal grinding and polishing would be needed afterwards. The bars were then ground and polished on their outer surface in a few steps, using 1200 to 4000-grit paper, and a mirror like finish was obtained on the outside surface.

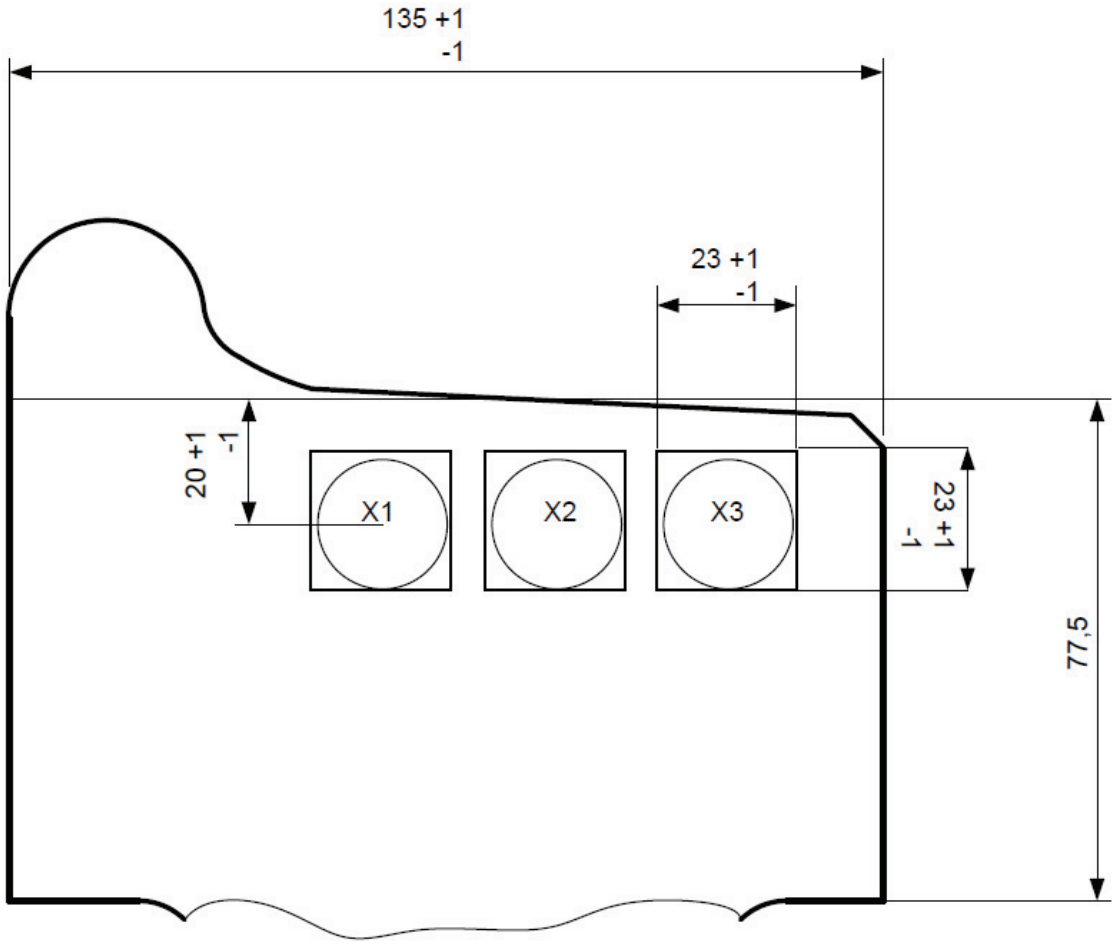

Figure 3.4: *Wheel rim cross section. The sketch describes how samples were extracted from the wheel for manufacturing of thin walled test bars (in mm). All bars were taken approximately* 20*mm below the running surface*

3.5 Microstructural characterisation of R260 rail material (Papers C and D)

For the R260 rail material, focus was on comparison of deformed test bars in the lab versus field samples (paper C). Hardness distribution, flow lines and pearlite orientation were measured. Subsequent characterisation of the microstructure included Transmission Electron Microscopy (TEM), to measure the microstructural parameters: interlamellar spacing, ferrite lamellae thickness and dislocation density. These were then used to evaluate the strength of the material at various shear strain levels.

In order to have an even material quality (microstructure), two symmetrically positioned samples from the rail corners were extracted from virgin rail heads, as shown in figure 3.5, with the distance below rail surface to be kept as low as possible and a centre line depth of around 15 mm. Hardness of such rail head from a previous examination is

also shown. The test bars used for predeformation were turned between centers to the dimensions in figure 3.6. The predeformation experiments of the test bars used have been further described in [3].

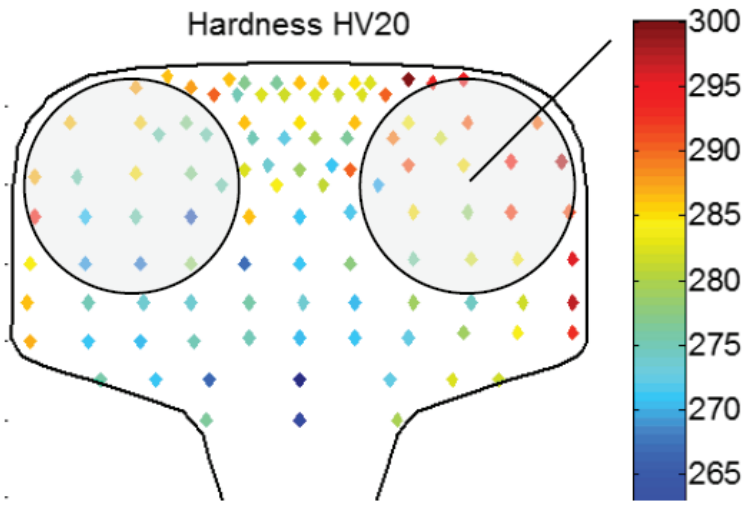

Figure 3.5: *Extraction of R260 test bars*

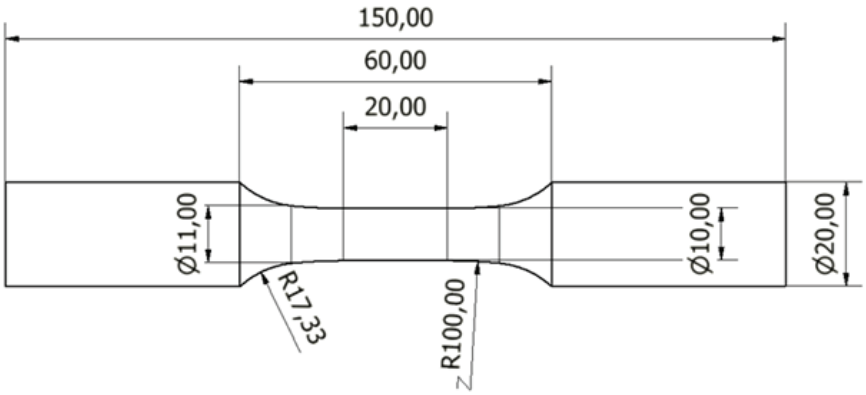

Figure 3.6: *Geometry of R260 test bars (in mm)*

Rail pieces (Rail A and Rail B) were taken at two locations along the main railway line in Sweden, between Stockholm and Gothenburg, in the region Jonsered Östra. The rails have been subjected to the similar mixed traffic conditions, with one main direction due to the double tracks. Two positions are considered for each rail, at the top and at the gauge corner, according to figure 3.7.

Three different methods are used to characterise the material and its microstructure: First, hardness measurements are used to evaluate the local inelastic material behaviour at different depths in the rails. Secondly, shear lines are used to quantify the amount of accumulated shear. Finally, the microstructural deformation state can be quantified by evaluating the orientation distribution of the cementite lamellae.

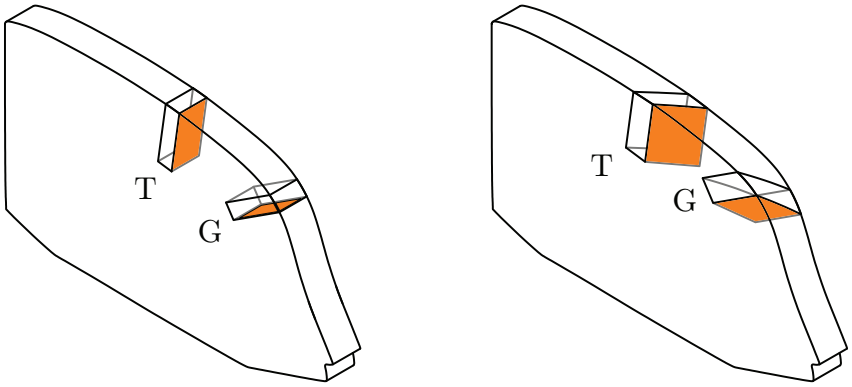

a) 90° samples. b) 45° samples.

Figure 3.7: *Samples extracted from the top of the rail (T) and gauge corner (G) with two orientations with respect to the rail longitudinal direction. The orange coloured sides denote the surfaces studied.*

Both the Vickers and the Knoop method were used to evaluate the material hardness. Due to the strong gradients close to the surface, the Knoop method was chosen with a 10 g load (HK0.01), as this allowed for closer spaced indents with a sufficient size for optical measurement. These measurements were conducted on an Struers DuraScan 70 hardness machine, using a 60× objective lens. A global hardness map of the rail was obtained using a Vickers hardness indenter with a 10 kg load (HV10). During the second study of R260 (paper D), microhardness measurements on the test bar sample were done using Vickers 500 g load (HV0.5).

Transmission electron microscopy (TEM) was used to measure the microstructural parameters of the R260 material, after it was deformed in a biaxial machine with the aim to corelate them with various levels of shear strain (paper D). Standard grinding and electro-polishing (10 % perchloric acid in ethanol) procedures were used to prepare specimens for investigation in a JEOL 2000FX TEM. The interlamellar spacing (ILS), and ferrite and cementite lamellar thickness were measured. For each sample, data was collected from 30 measurements on randomly chosen areas. Dislocation configurations and densities were examined using the TEM at 200 kV. The dislocation density was determined by the line intersection method applied to TEM micrographs.

4 Results

This section presents a selection of the main results and analysis, for the performed experiments.

4.1 Microstructural degradation of R8T wheel material (Paper A)

The results of this section are described in detail in paper A. The effect of the heat treatments is shown in figure 4.1. The initial hardness value for the virgin material, also called "undeformed" R8T is around 260 HV10 (figure 4.1a), around 274 HV10 for the monotonically strained condition (figure 4.1b) and around 309 HV10 for the cyclically strained R8T (figure 4.1c).

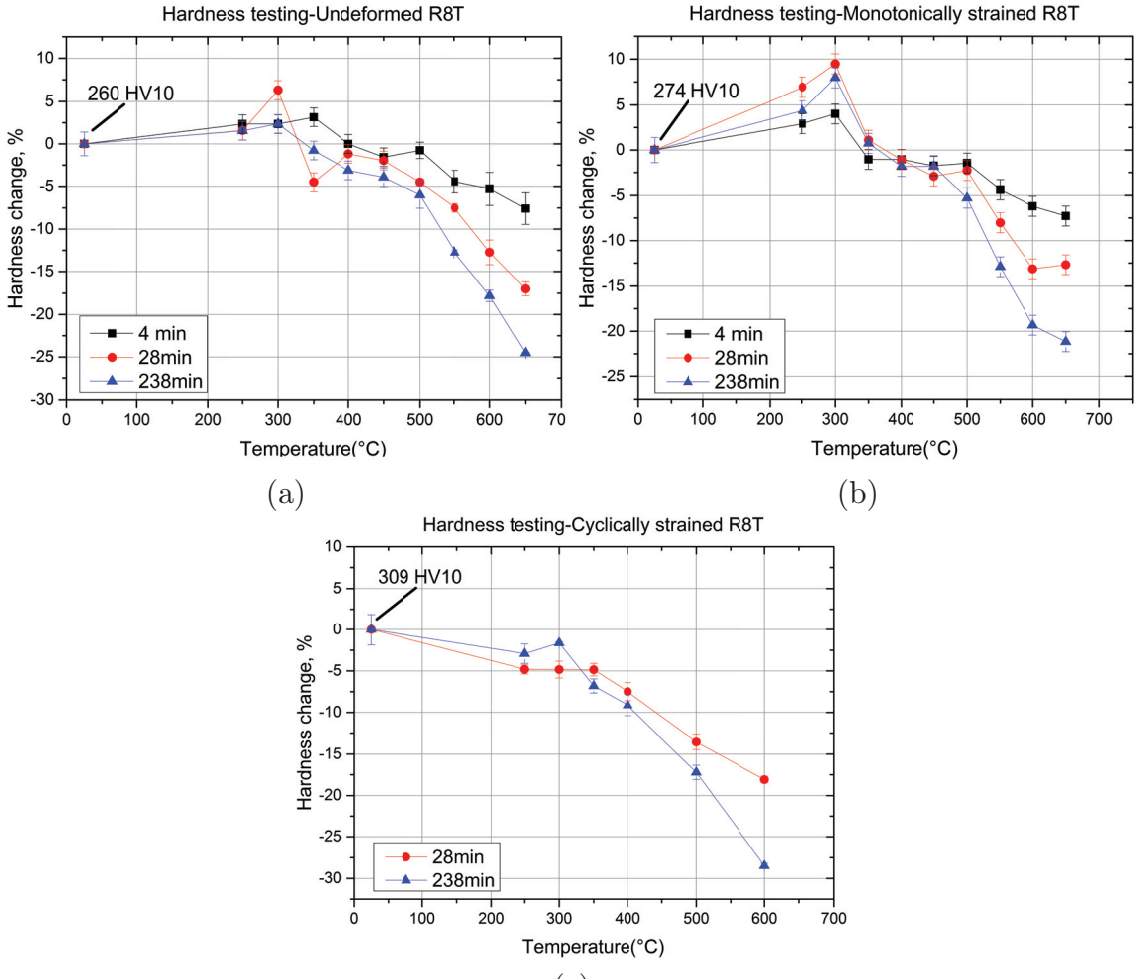

Figure 4.1: *Hardness change after heat treatments of R8T material for (a) undeformed (b) monotonically strained and (c) cyclically strained*

From figures 4.1a-b it is clear that a hardening process is taking place around 300°C for the undeformed and the monotonically strained materials whereas for the cyclically strained material (figure 4.1c), this is less obvious. The main reason behind this hardening is strain ageing. When the material is monotonically strained and then annealed, static strain ageing gives a higher hardening contribution compared to the undeformed, because of its larger dislocation density. The dislocations in the cyclically strained material are possibly annihilated during annealing. This would counteract the effect of static strain ageing, thus showing a lower hardening effect. The hardening seems to be more pronounced when the material is subjected to 28 min heat treatments in the cases of virgin and monotonically strained material. At temperatures above 350°C, increasing softening occurs for all three time durations. For the temperature range 400-450°C, both of the above conditions have lost a few percent in hardness, whereas the cyclically strained material undergoes severe softening in this temperature range. After 500°C severe softening for all conditions is observed. It can be concluded from the above observations, that exposure to high temperatures has a large influence on the hardness of the material. The above results indicate that cyclic plastic deformation combined with exposure to high temperatures, for example after excessive braking in train operation, will have a great impact on the mechanical properties of the material.

The initial microstructure of R8T is shown in figure 4.2.

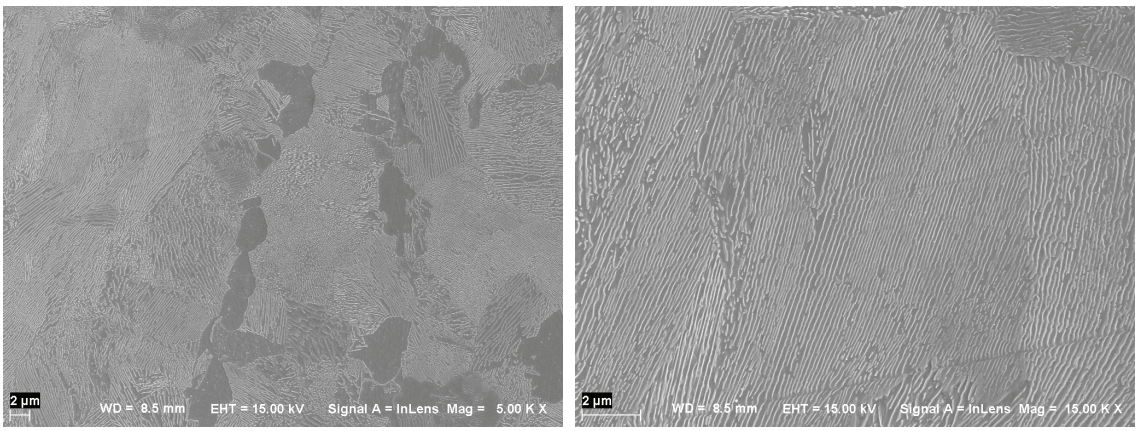

(a) (b)

Figure 4.2: *SEM microstructural overview of the undeformed R8T at two magnifications*

The interlamellar spacing was calculated at three different depths using such SEM micrographs. The mean true interlamellar spacing values along with the standard deviations appear on table 4.1. It is clear that the spacing is finer close to the surface and gets coarser as we move further down from the surface of the wheel. One would expect the R8T with the higher carbon content to have a finer spacing [31], but cooling rates could have stronger effect.

The ferrite content is shown in figure 4.3. It increases from 8.2 at 20 mm depth up to 12.2 vol.% at 60 mm depth for R8T and correspondingly from 11.3 to 14.4 vol.% for R7T.

Table 4.2 shows the hardness measurements at the three depths. It is clear that the material softens with increasing depth since the free ferrite content increases and the

Table 4.1: Mean true interlamellar spacing (nm)

Depth(mm)	R8T	St. deviation	R7T	St. deviation
20	132	5.6	125	8.7
40	145	9.5	134	4.1
60	157	8.7	146	12.8

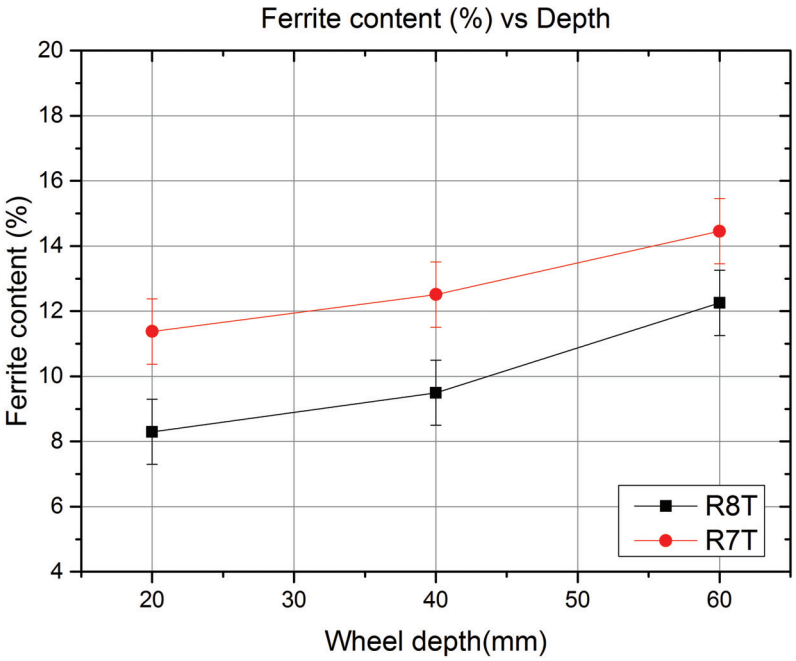

Figure 4.3: *Ferrite content with increasing wheel depth*

interlamellar spacing increases. R8T has slightly higher hardness than R7T as expected. An unexpectedly high hardness value for R7T at 60 mm depth was measured, but is thought to be due to measurement inaccuracy and sampling combined with a larger standard deviation in the R7T interlamellar spacing at 60 mm depth.

The SEM investigation of the undeformed R8T material, after the annealing treatments, showed that the pearlite lamellas start to break up around 450°C (figure 4.4) with a more pronounced effect for longer durations. This could explain the small drop in hardness as seen in figure 4.1a. The same degree of spheroidisation happens earlier for the monotonically strained material at around 400°C. It appears that pre-deformation of the material has an effect on the microstructure degradation.

Higher temperatures and longer times allow for stronger spheroidisation which correlates to the increasing drop in hardness. It is shown in figure 4.5 that severe spheroidisation is taking place for temperatures above 500°C. Similar results were obtained for the cyclically strained R8T material.

Table 4.2: Hardness with increasing depth

Hardness (HV10)		
Depth (mm)	**R8T**	**R7T**
20	268	266
40	254	252
60	242	253

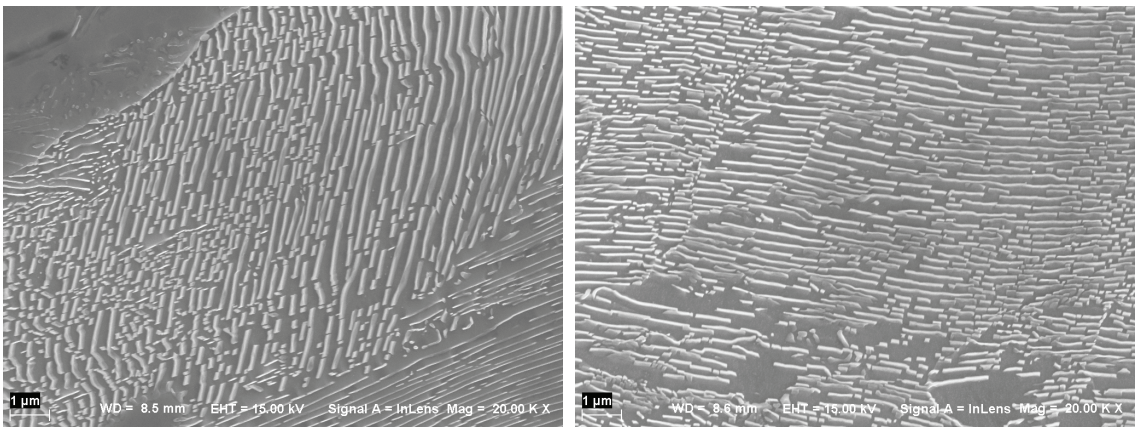

(a) (b)

Figure 4.4: *SEM micrographs of the R8T material heat treated for 238 min (a) undeformed, heat treated at 450°C and (b) monotonically strained, heat treated at 400°C*

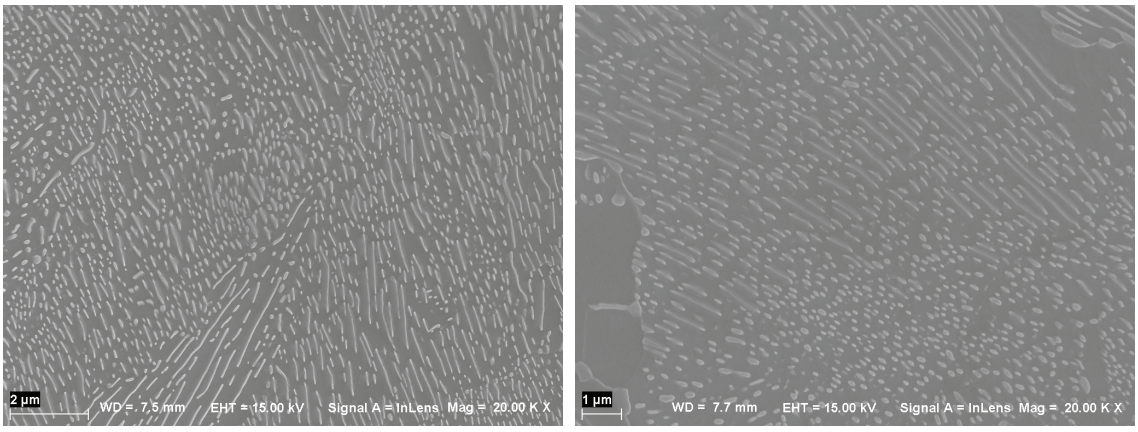

(a) (b)

Figure 4.5: *SEM micrographs of the monotonically strained R8T heat treated for 238 min at (a) 500°C and (b) 600°C*

It is obvious from these micrographs that the combined influence of plastic deformation and thermal exposure causes a degradation of the microstructure. First the lamellas break up from the deformation and the heat treatment and then through further coarsening,

spheroidisation of the cementite particles occurs. This in turn causes the decrease in room temperature hardness that is observed, which becomes more severe for larger durations and higher temperatures.

4.2 Elevated temperature behaviour of R7T wheel material (Papers A and E)

To complement the above hardness measurements with behaviour at elevated temperatures, different fatigue tests were performed on R7T. These are described in papers A and E. Initially uniaxial low cycle fatigue tests at elevated temperatures were done (paper A). These experiments showed the strong influence of temperature on the peak stress development, see figure 4.6 (the equivalent graph with the trough stress development during the compressive segments of the test shows very similar results with the lines mirrored towards the negative values).

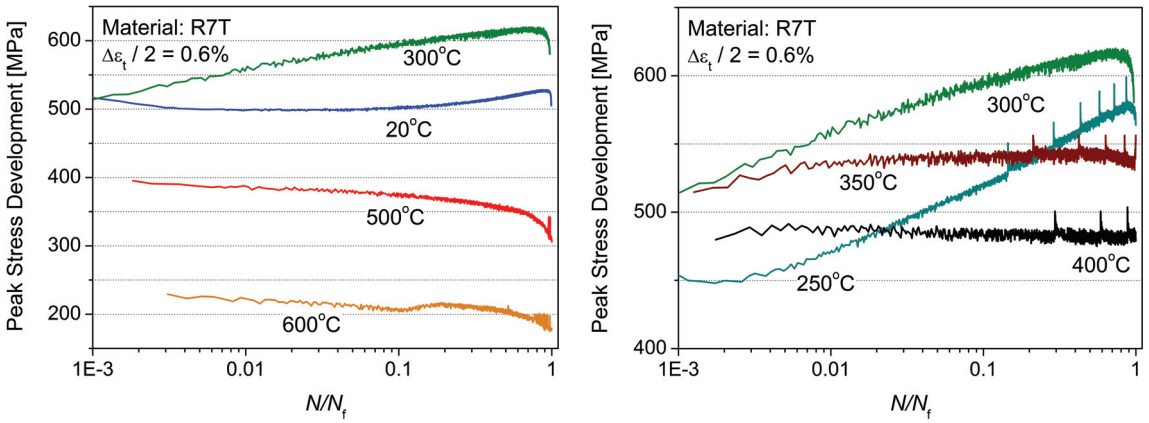

Figure 4.6: *Peak stress development in the interval 250-600°C with a room temperature curve also reported for reference*

At 300°C, there is a strong initial hardening that decreases to slight hardening during the remainder of the fatigue life (seen in the range 10–80 % of the fatigue life, thereafter major cracks influence the stresses registered). The mechanism behind this hardening is dynamic strain ageing, with locking of dislocations by interstitials [49]. To examine the temperature range where DSA is active more closely, complementary tests at temperatures from 250°C to 400°C were done. At 250°C, the hardening is even greater than at 300°C and it appears later in the fatigue life. At 350°C, thermal softening, i.e increased mobility of dislocation following increased thermal activation, sets in and at 400°C this mechanism dominates, giving lower peak stresses with time, as compared to the room temperature behaviour seen in figure 4.6a. At the two higher temperatures, 500°C and 600°C, the material exhibits considerably lower peak stresses and cyclically softens during the fatigue life, as a result of combined thermal softening and microstructural degradation. These results agree with the loss in room temperature hardness due to microstructure degradation

(spheroidisation) giving severe softening after exposure to higher temperatures.

In figure 4.7, cyclic stress-strain curves from the ratcheting tests are shown for each temperature (engineering stress-strain). After the first few cycles a constant ratcheting rate is reached until the end of the test for all temperatures. At 300°C, the material exhibits the lowest strain out of the four temperatures examined. Half of the final racheting strain is reached already in the first cycle, thereafter dynamic strain ageing contributes to hardening, that limits the ratcheting rate. This was also observed in previous work of the authors for strain controlled cyclic tests at this temperature [58]. The highest strains are achieved for the two higher temperatures.

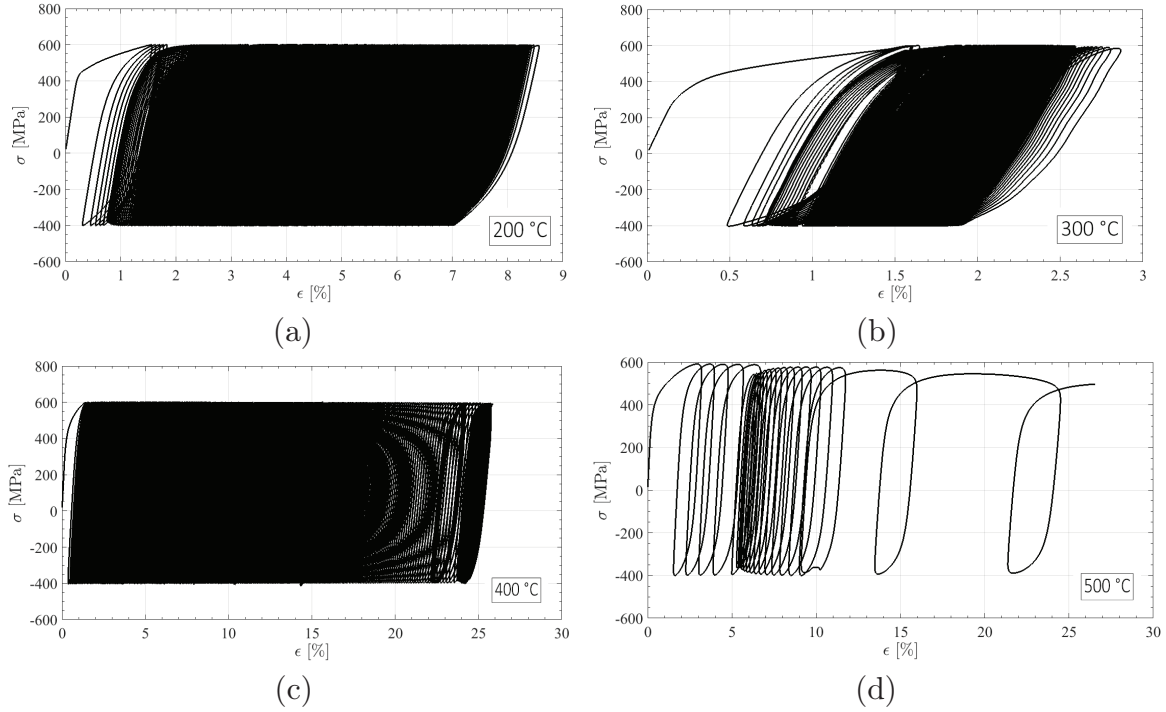

Figure 4.7: *Stress-strain curves of uniaxial ratcheting tests at elevated temperature*

The fatigue life of the test bars was evaluated for each temperature and it is shown in figure 4.8. At 300°C, the material exhibits the longest fatigue life, whereas at higher temperatures where thermal softening takes place, the fatigue life decreases rapidly.

The equivalent von Mises peak stress development is shown in figure 4.9. All conditions exhibit a very rapid initial hardening within the first one or two cycles of the test. After that, a differentiation in behaviour occurs depending on the temperature. At room temperature, there is little further hardening after the initial cycles. At 300°C, a continuous hardening can be seen throughout the fatigue life, however with a decreasing rate. At 0.6 % the slope in the log(N) plot is constant until failure, whereas at 1.0 % there is a saturation and then decrease in peak stress before failure. At 200°C the behaviour is similar, but with a lower rate of hardening and lower stress levels. At 400°C a slight variation in peak stress levels between each cycle is observed, with some very slight hardening through the fatigue life and softening towards the end. The cycle to cycle variation visible at the higher temperatures is thought to result from the temperature

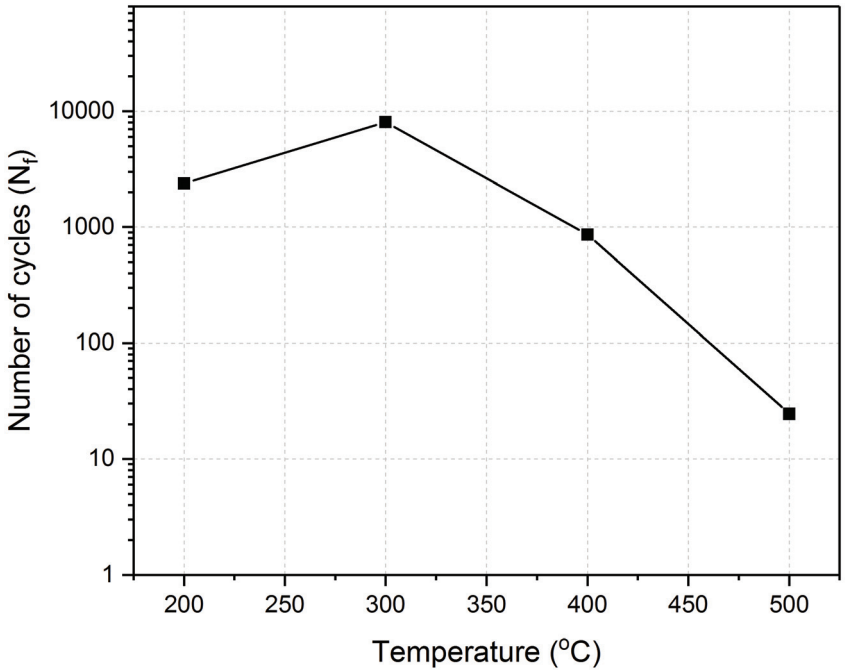

Figure 4.8: *Fatigue life, represented as number of cycles to failure, Nf, of ratcheting tests at the four temperatures tested*

control, since no thermal strain compensation was applied. The total strain control thus imposed a slightly varying mechanical strain amplitude. Generally fatigue life is much shorter for the tests run at 1.0 % strain amplitude.

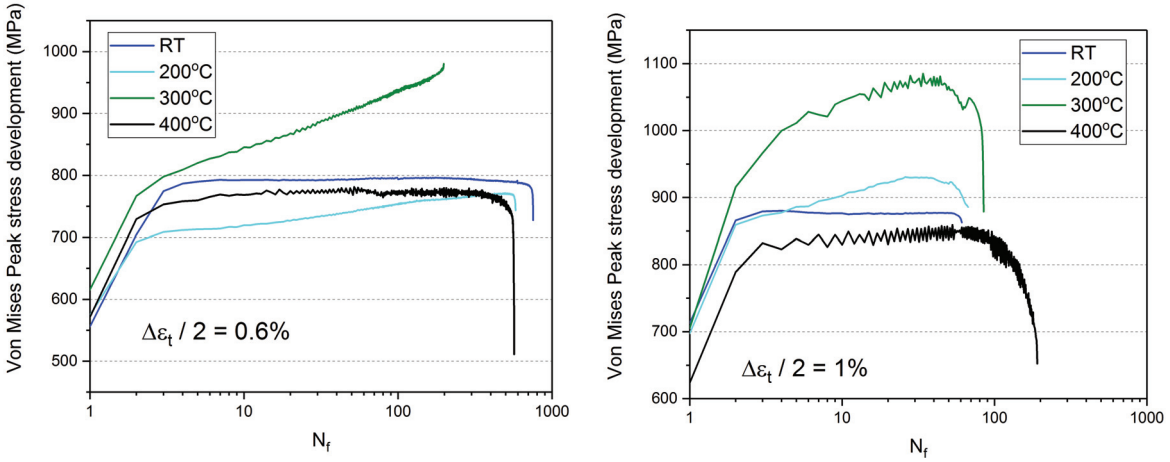

Figure 4.9: *von Mises peak stress development for the various temperatures tested versus the fatigue life. Strain amplitude of (a) 0.6 % , and (b) 1.0 %.*

4.3 Quantification of spheroidisation (Unpublished)

The study in this section does not appear on any appended paper. As observed in the micrographs above, not all areas of the microstructure gets spheroidised at the same time. Some areas remain intact even after the longest duration in the furnace. In an attempt to quantify the amount of spheroidisation, a small scale study was initiated with the focus to create a Matlab script to perform image processing in SEM images to quantify the spheroidisation, as described in the experimental section of this thesis. A typical image after processing appears in in figure 4.10.

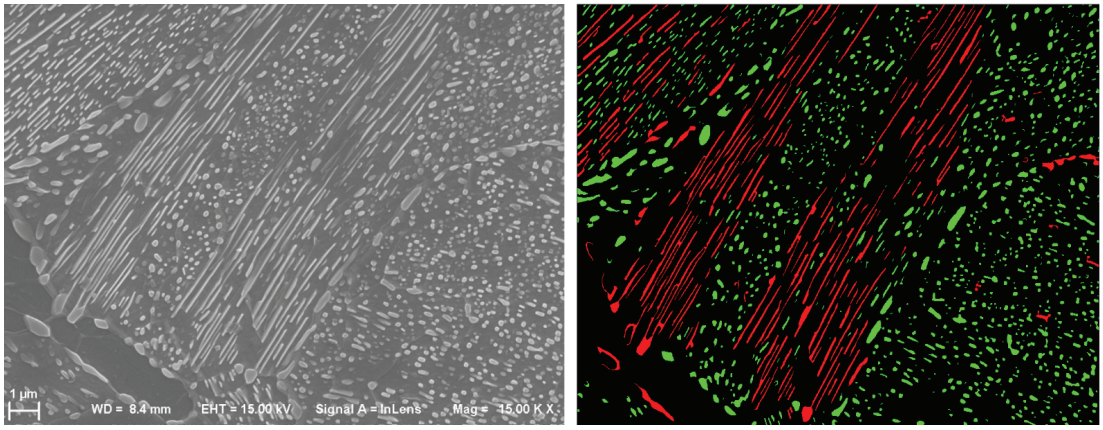

(a) (b)

Figure 4.10: *Visual result of the script developed. Original image on the left, processed image on the right (red regions are lamellar cementite defined as L/W>8, green are globular).*

For this classification, an aspect ratio larger than 8 was used, L/W>8. Regions above 8 are considered lamellar cementite (shown in red) and regions below 8 are considered globular (shown in green). After analysing the SEM images as shown above, the program gives the calculation of the total cementite fraction, and the relative content of globular and lamellar structure. Total cementite fraction ranges from around 15 % after heat treatment at 250°C to 9 % after annealing at 650°C, which is closer to the theoretical value of 8.1 % calculated in section 3.3. This is because of the angle at which the lamellae are observed in the 2D sections, meaning their thickness is overestimated. This is why thinning is employed. The idea behind the thinning of the cementite regions is to reduce the area of the regions, since it is hitherto overestimated. This overestimation is more pronounced in fully lamellar cementite. The more the material spheroidises, the less the overestimation, leading us close to the expected value. The thinning is currently done statically (same thinning for all images of a set); the program is set to morphologically thin the regions once. To get an accurate result, it would be preferable to do this in an adaptive way. Ideally, the thinning procedure should be done so that the measured cementite percent in the image matches the nominal value. There are also some mis-classifications in some of the images as seen in figure 4.10. These are usually very few and many images per sample are used to avoid these few errors affecting the overall calculation.

The trend of the cementite spheroidisation and the amounts of globular and lamellar cementite at various temperatures can be seen in figure 4.11.

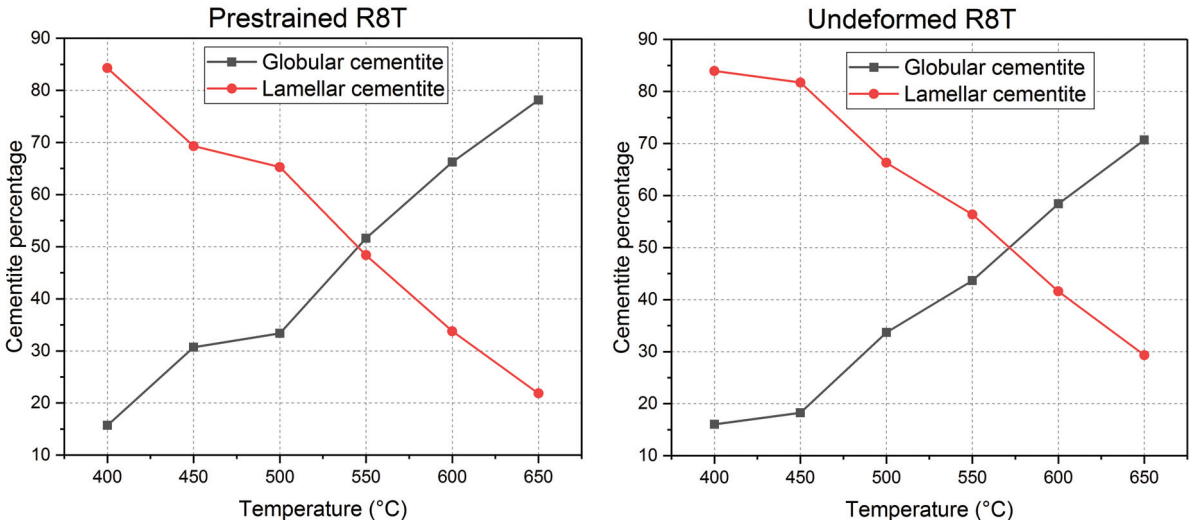

(a) (b)

Figure 4.11: *Cementite spheroidisation for different temperatures for pre-strained and undeformed material*

As it is shown in figure 4.11, pre-straining seems to make the spheroidisation more pronounced compared to the undeformed material. It is clear that spheroidisation reaches around 80 % for the pre-strained material and 70 % for the undeformed, when the samples were heat treated at 650°C. Overall the trends seem reasonable as with increasing temperature, more material starts spheroidising.

4.4 EBSD analysis (paper B and unpublished)

This section includes an extended selection of results, part of which appear in paper B. Wheel material R8T was examined in this EBSD analysis. As a reference, an undeformed specimen was examined to evaluate the initial state of the material microstructure after production. A random area was selected without taking into account any specific pearlite colony or other microstructural features. The grain boundaries map along with the kernel average misorientation map is shown in figure 4.12. One can observe from these that a lot of sub-grain boundaries exist (showing as red lines on grain boundary maps), along with a strong local misorientation that suggests a very high dislocation density is present in the initial microstructure that is contributing to the material's initial mechanical properties.

In figure 4.13, an SEM micrograph along with the inverse pole figure map is shown for R8T after annealing at 300°C.

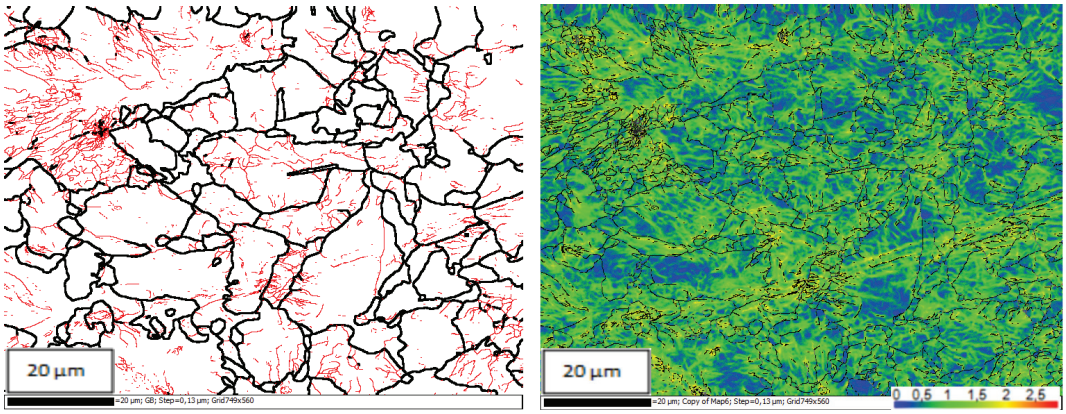

(a) (b)

Figure 4.12: *Microstructural mapping of undeformed R8T material at room temperature using the grain boundary plot with red lines for low angle boundaries(LAB) between 2-10° and black lines for high angle boundaries >10° (HAB) (a) and Kernel average misorientation map (b) using orientations up to* 2^{nd} *neighbour shell.*

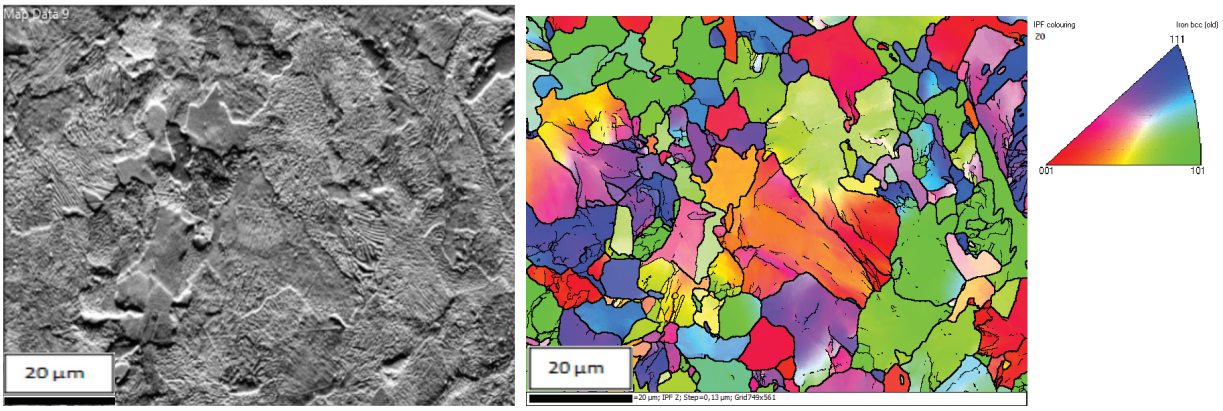

(a) (b)

Figure 4.13: *Microstructure of undeformed R8T material after annealing at 300°C using the forescatter detector (left) and texture mapping using the inverse pole figure (IPF) colour code of the crystallographic normal vector (right)*

Pearlite colonies appear to have orientation gradients as reported in literature, while pro-eutectoid ferrite grains are shown with a single colour and thus a single orientation. The grain boundaries and KAM for this condition are shown in figure 4.14. No apparent microstructural degration takes place at this temperature, but it is clear that dislocation density has dropped significantly after annealing. Ferrite grains that appear mostly blue in the KAM plot seem to have no sub-grain boundaries and most of these low angle boundaries are concentrated in the pearlitic colonies.

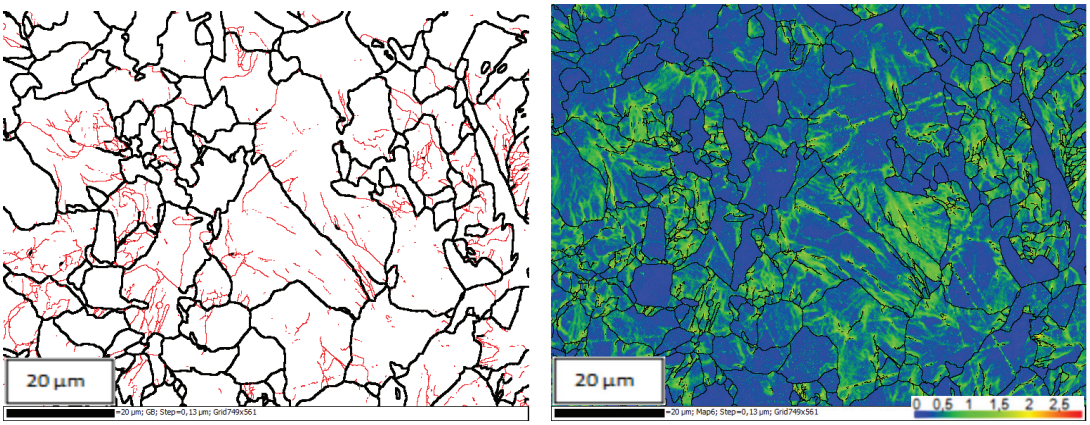

(a) (b)

Figure 4.14: *Microstructural mapping of undeformed R8T material after annealing at 300°C using the grain boundary plot with red lines for LAB between 2-10° and black lines for HAB >10° (left) and Kernel average misorientation map (right) using orientations up to 2nd neighbour shell*

When annealing at even higher temperatures at 500°C spheroidization starts to occur. In figure 4.15, a micrograph of this temperature is shown with an IPF map. Spheroidised colonies appear to start losing the previous orientation gradients seen in the pearlite colonies (c.f figure 4.13b). Ferrite grains appear with no local misorientation (blue colour) in the undeformed material KAM maps, whereas in the pre-strained they seem to have some degree of misorientation and larger part of the field of view is showing as green. One possibility is, since pre-straining makes the material more prone to spheroidisation as shown previously from the heat treatments, cementite carbon might be diffusing from previous pearlite colonies to the pro-eutectoid ferrite grains and precipitate there. This is still under evaluation and further analysis of the results is necessary.

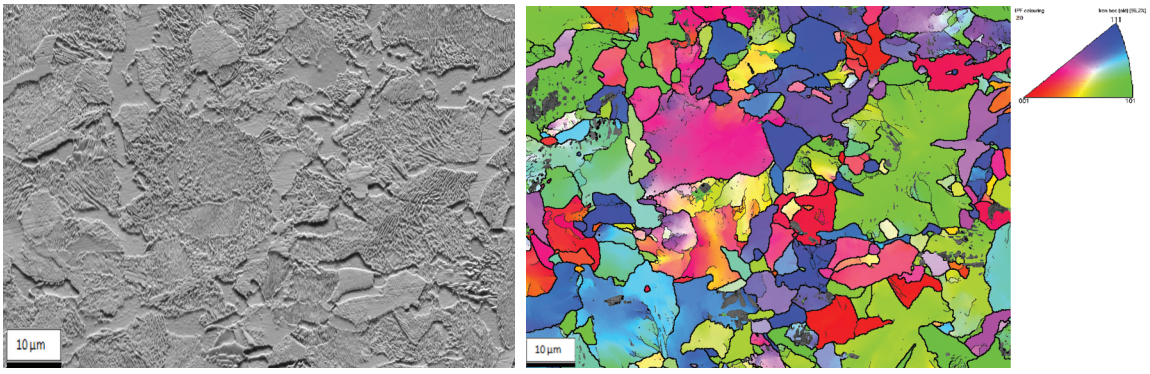

(a) (b)

Figure 4.15: *Microstructure of undeformed R8T material after annealing at 500°C (left) and texture mapping using the inverse pole figure (IPF) colour code of the crystallographic normal vector (right)*

The same investigation was also performed for the monotonically strained R8T. A

comparison of the grain boundary and KAM maps between the two conditions for various temperatures is shown in tables 4.3 and 4.4, that will allow for some better overview and comparison. All the samples appearing in tables 4.3 and tables 4.4 were heat treated for 4 hours. The prestrained material seems to have a higher number of subgrain boundaries that don't seem to anneal as fast as the undeformed material, even at the higher temperatures.

Table 4.3: Grain boundary maps comparison between undeformed and monotonically strained R8T at various temperatures (red lines for LAB between 2-10° and black lines for HAB >10°), scaling as in figures 4.12, 4.14

	300°C	500°C	650°C
Undeformed	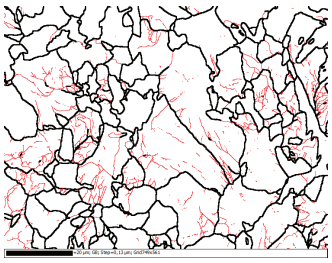	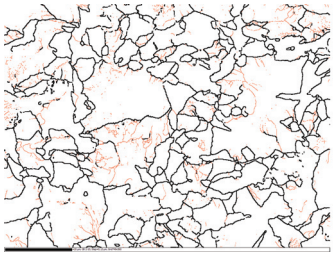	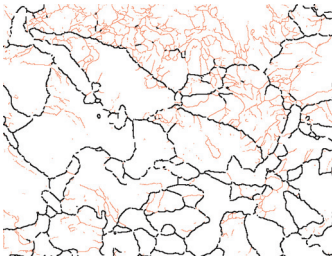
Monotonically strained	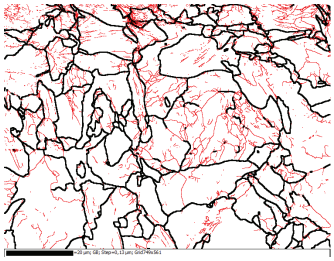	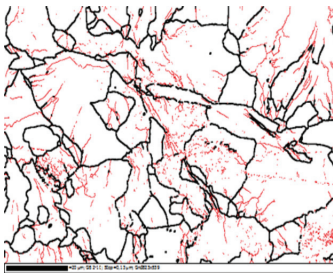	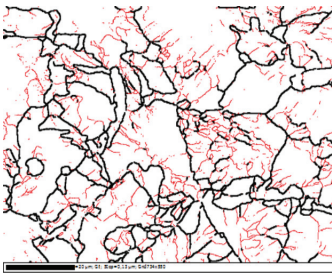

Table 4.4: Kernel average misorientation maps comparison between undeformed and monotonically strained R8T at various temperatures, colour scale and scaling as in figures 4.12, 4.14

	300°C	500°C	650°C
Undeformed	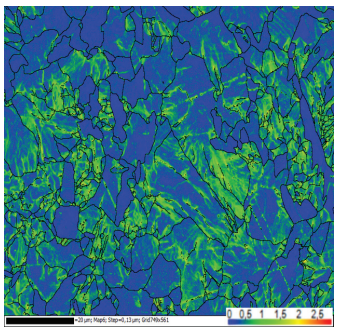	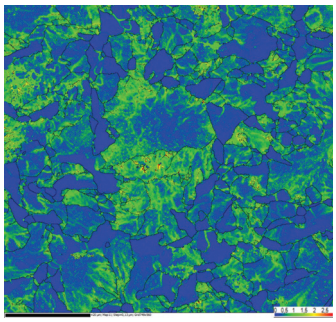	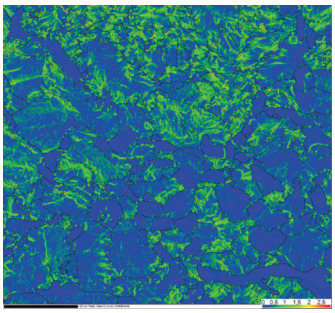
Monotonically strained	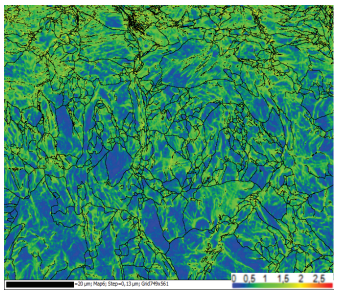	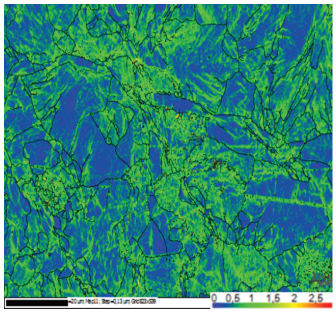	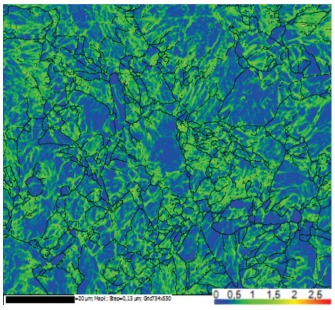

4.5 Comparison between biaxially deformed R260 and field samples (paper C)

The results in this section are part of paper C. Hardness indents are made on one disc from each bar, in a radial pattern with 8 points for each radius. The results from this are shown in figure 4.16. The differences between the bars show a spread of about 20 HV1, and a fairly linear increase of hardness with radius is obtained. Extrapolating to the centre of the bars gives a centre hardness of between 280 and 300, while a maximum hardness of about 360 is obtained close to the surface.

As previously mentioned, the critical area for RCF in rails is the surface region close to the running band. We therefore consider the hardness variation with depth for the two analysed regions, the gauge corner (G) and the top of the railhead (T) in figure 4.17. The average hardness and standard deviation at a radius of 4.5 mm and outwards of the test bar B1, based on 64 indents, are also given for comparison.

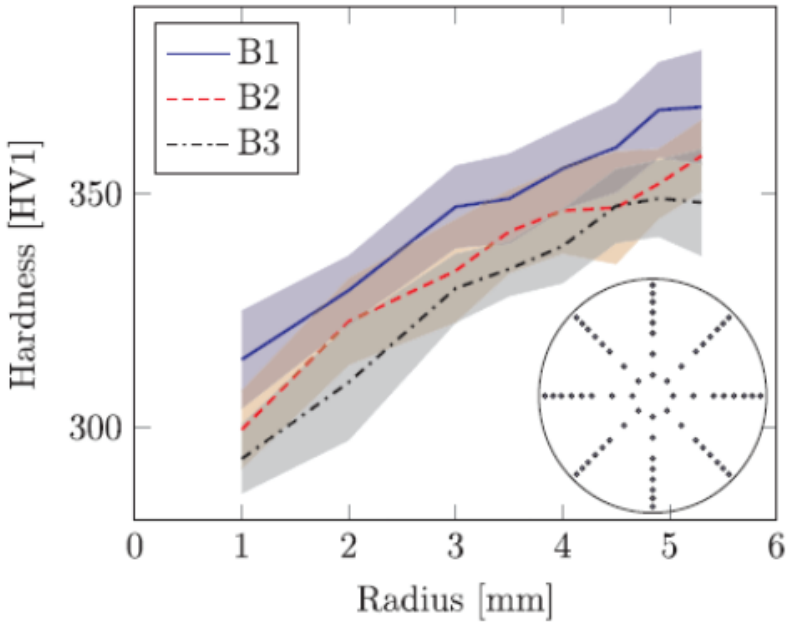

Figure 4.16: *Hardness variation between test bars subjected to the same loading. The three bars used are named as B1-B3*

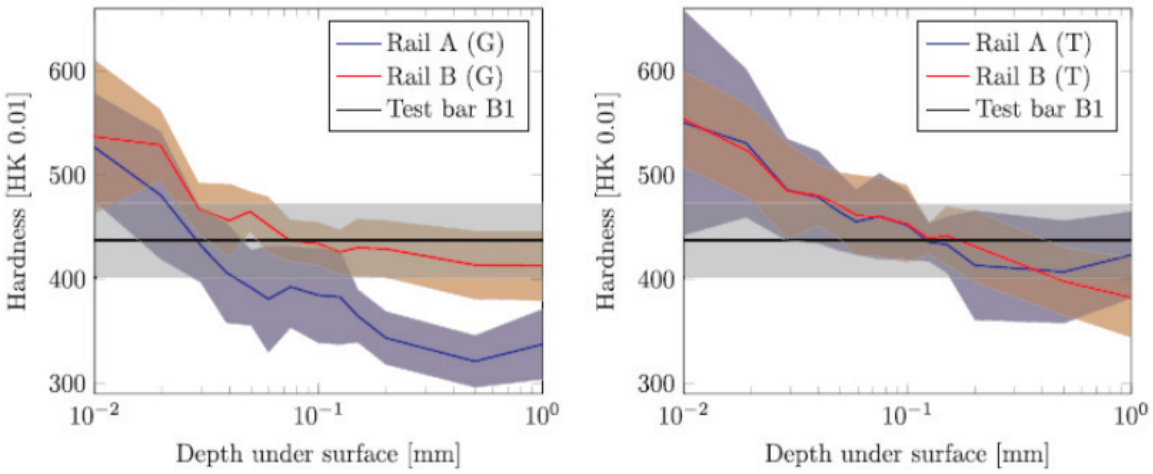

Figure 4.17: *Hardness depth variation, filled region indicate ± one standard deviation*

For all rail samples, the Knoop hardness values close to the surface are approximately 550, and show a steep gradient during the first 100 μm. The hardness deeper into the rail is at about 400 at 1 mm for all samples except the gauge corner of Rail A. For this sample the interior hardness is lower, and the gradient is very steep within the first 60 μm. For the other samples, their hardness at about 100 μm corresponds to the hardness of the B1 bar.

The next method of comparison was the shear line method. Four of the investigated rail samples show very distinct shear lines, see figure 4.18.

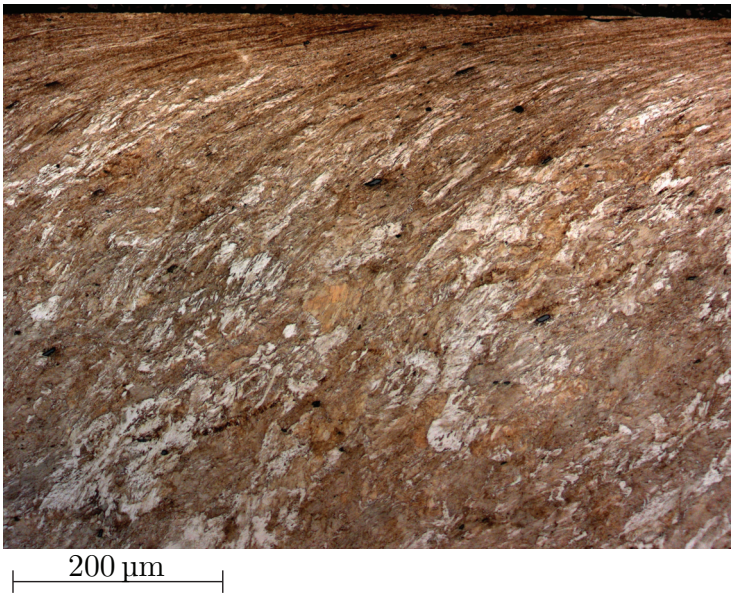

Figure 4.18: *The deformed surface layer of Rail B at the gauge corner (45°)*

The flow lines are most distinct from about 30 μm down to about 100 μm. Closer to the surface the lines are difficult to identify in some cases, and some waviness can be observed as a consequence of local flow variations. Deeper into the rail, the lines are also less identifiable and are mostly determined by the elongation of the grains. The calculated shear measure γ is shown in figure 4.19, where the measurements from the first 10 μm have been excluded due to the large uncertainties in these measurements.

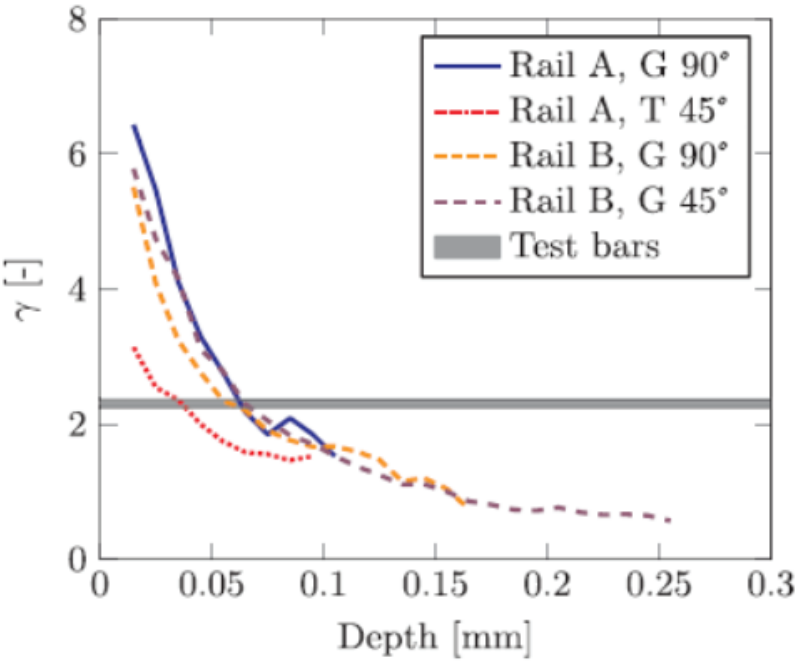

Figure 4.19: *Shear measure γ, excluding the first 10 μm*

The span of the measured average shear in the bars B1-B3 is collected in the grey band in figure 4.19. The shear in the test bars is equivalent to the strain levels at a depth of 0.07 mm for the majority of the rail samples with visible shear lines. The figure also shows that the spread between the test bars is much smaller than the variation between the rails.

Finally, the last measure was to analyse lamella orientation in the test bars and field samples. Both mean lamella angles and distribution were evaluated. For the rail shown in figure 4.18, the lamella orientation is plotted at different depths in figure 4.20. The dashed line shows the average lamella orientation of the predeformed test bars for comparison.

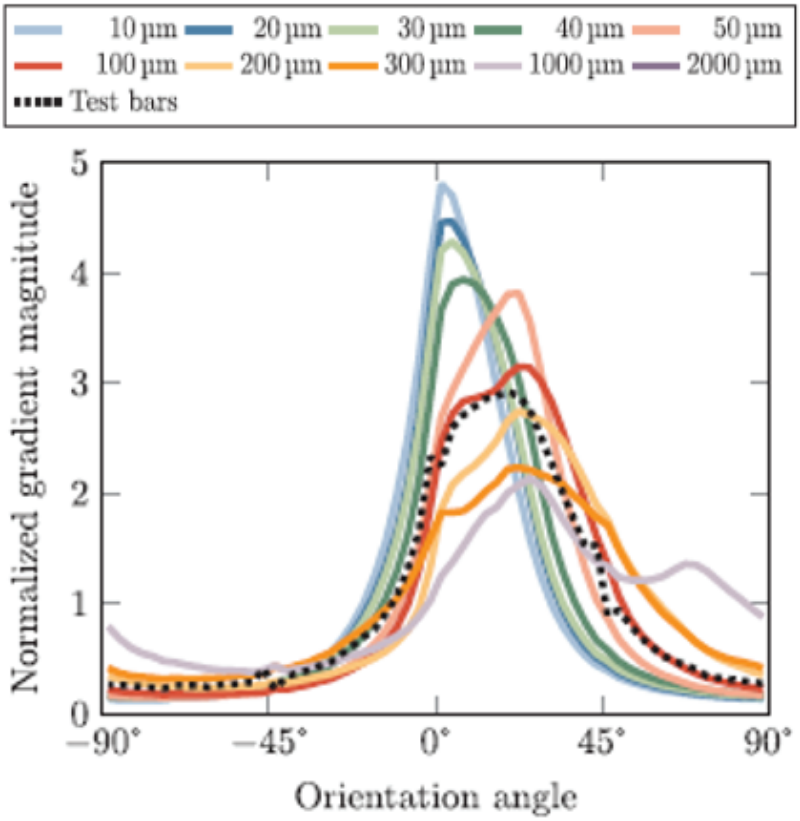

Figure 4.20: *Orientation of lamellae of Rail B at the gauge corner (45°)*

The heavily sheared microstructure as indicated with the flow lines is also apparent in the lamella orientation distributions with a very sharp peak closer to the surface. The average orientation angle increases with increasing depth and the distribution becomes more uniform.

4.6 R260 evaluation of local strength (paper D)

Below are results taken from paper D. Samples for characterisation were extracted from test bars that were deformed in a biaxial machine using torsion-compression as described

in the previous section. Depending on the position of the sample in these test bars, different shear strain levels were calculated. A surface pattern consisting of a regular grid was imprinted on the specimens before the test, and the angle between these lines was then used to compute the shear strain of the test bars at different positions according to the following formula:

$$\gamma = \frac{\tan(90 - \theta)}{R} r \tag{4.1}$$

where θ is the angle measured at the outer surface of the test bars (see figure 4.21), r is the radius measured from the centre line of the bars and R is the final radius of the test bars after the end of the pre-deformation procedure. With this, 5 shear strain levels are selected from 0 to 1.6.

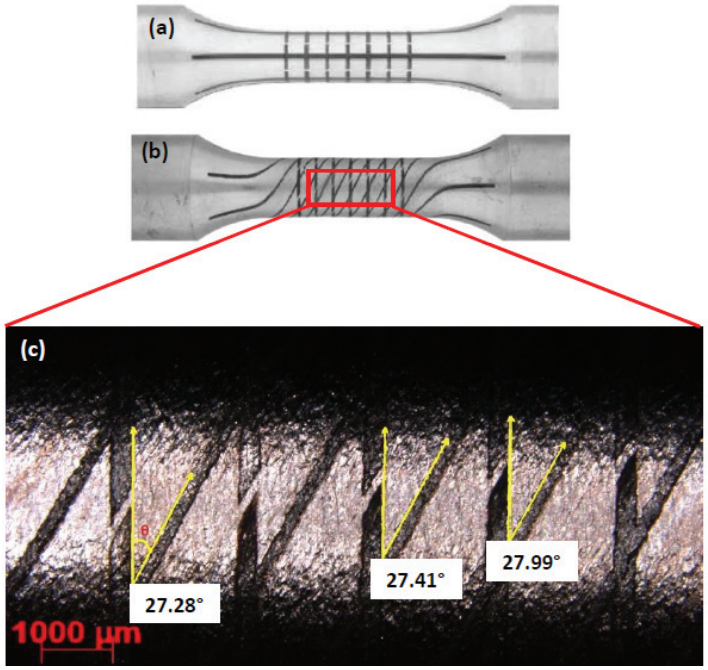

Figure 4.21: *Calculation of shear strain from outer surface of a test bar. Parallel lines are engraved on the test bar surface in a grid pattern before the deformation experiment (a) and the angle that is formed after the bars have been twisted is measured (b) Measurement is performed using a stereomicroscope (c)*

The initial pearlitic microstructure consists of alternating ferrite and cementite lamellae as shown in figure 4.22. The initial ILS, thickness of ferrite and cementite lamellae are 233 ± 39 nm, 193 ± 30 nm and 40 ± 6.5 nm, respectively. The black arrows in the figure also show the dislocation structures in the ferrite lamellae, and the average size of a pearlite colony is around 8μm.

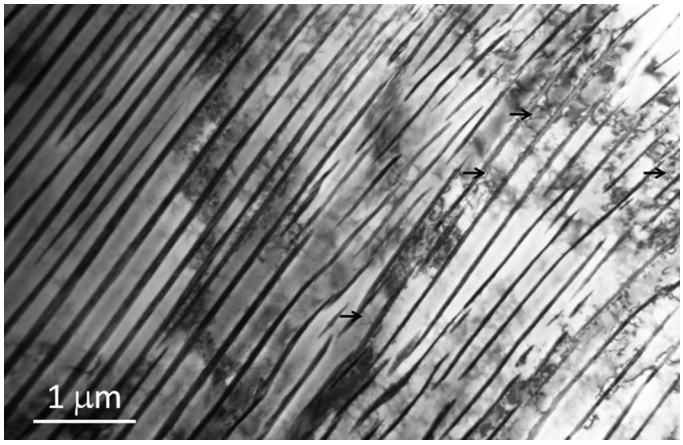

Figure 4.22: *Initial pearlitic microstructure with alternating ferrite and cementite lamellae where the black arrows show examples of dislocations in the ferrite lamellae*

By using such TEM microgaphs, the dislocation density was measured using the line intercept method. In the pearlitic steel with alternating ferrite and cementite lamellae, the deformation including yielding and plastic flow is largely controlled by processes occurring in ferrite, where the slip initially takes place in the ferrite lamellae, and then is transferred into the cementite lamellae [59]. Figure 4.23 shows the dislocations in the ferrite lamellae in the initial structure, with a dislocation density of $6{\times}10^{13}$ m^{-2}. The random dislocation lines can be observed as a result of the phase transformation and many bulging-out dislocations can be observed from the ferrite/cementite interfaces which may have its cause in the elastic incompatibility stresses between the two phases [60, 61, 35, 62].

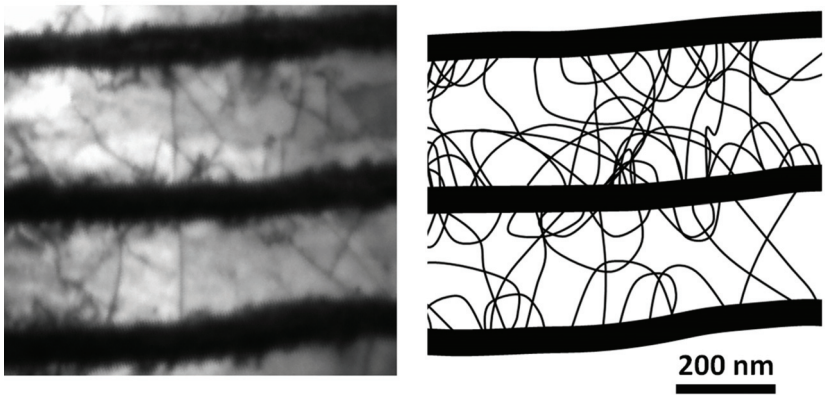

Figure 4.23: *TEM micrograph of the initial sample and a sketch of the dislocation structure in the ferrite lamellae*

The dislocation density and hardness are plotted in figure 4.24 versus the shear strain, showing an almost linear relationship.

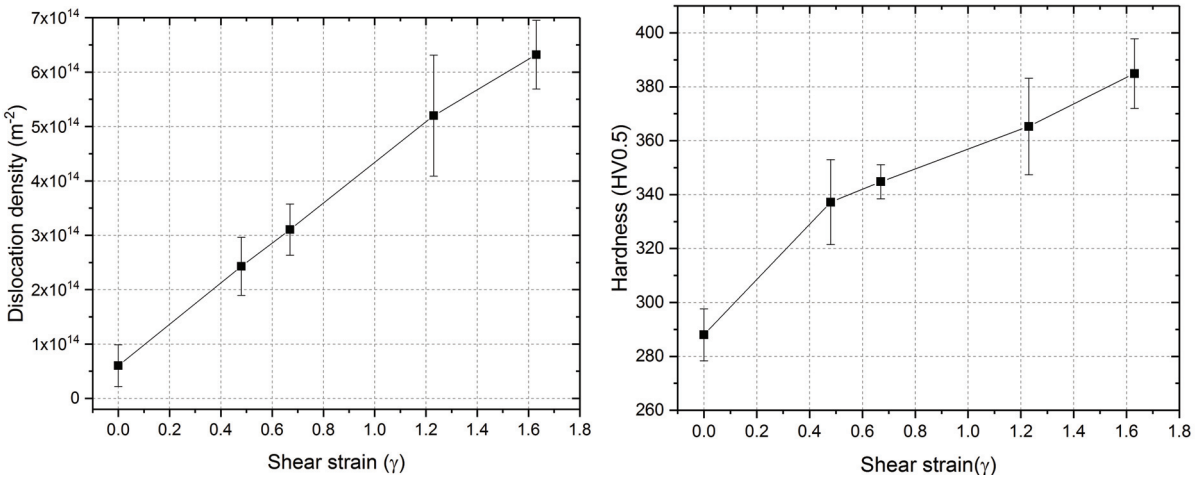

(a) (b)

Figure 4.24: *(a) Dislocation density in the ferrite lamellae versus the shear strain. The error bar shows the standard deviation and is determined using the values from around 30 areas(b) Hardness with increasing shear strain*

Using hardness measurements and the microstructural parameters (such as dislocation density, interlamellar spacing, etc) the flow stresses were calculated using formulas that are described in detail in paper [63]. These are plotted versus the shear strain in figure 4.25

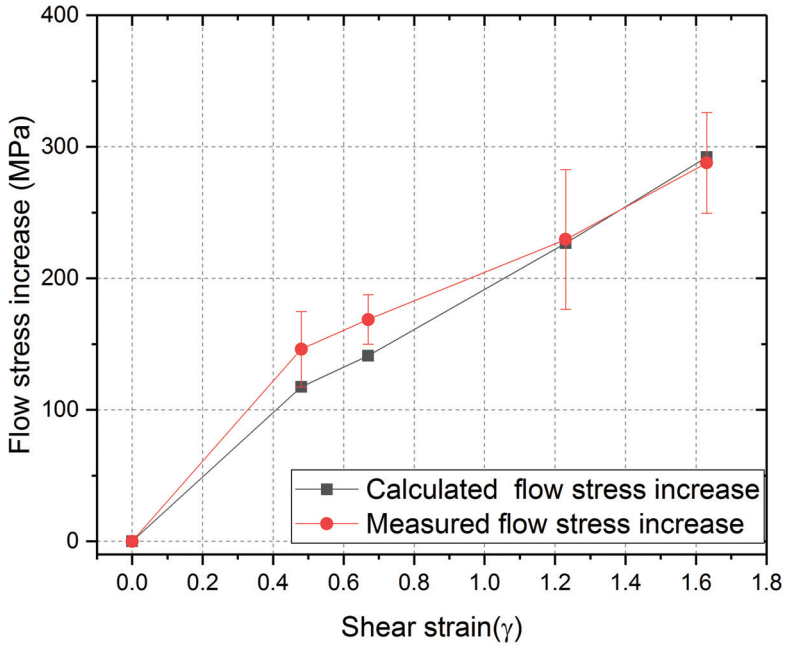

Figure 4.25: *The calculated and measured flow stress increases from microstructural parameters and microhardness versus the shear strain, respectively*

A good agreement can be observed between the calculated flow stress increase, quantified from structural parameters and the flow stress increase from microhardness measurement.

5 Conclusions and future work

The effect of combined thermal and mechanical loadings on the mechanical behaviour of near-pearlitic railway wheel steels was evaluated. The two materials R8T and R7T exhibit a slight difference in carbon content and may show a slight difference in hardness but otherwise behave similarly. The hardness tests performed at room temperature isolate the effect of microstructural degradation, while the elevated temperature low cycle fatigue tests shows the combined influence of microstructural degeneration and thermal softening due to increased thermal activation at higher temperatures.

Annealing treatments of R8T and evaluation of cyclic mechanical properties of R7T allowed for the following conclusions.

- The room temperature hardness increase after annealing at around 300°C is evident for both un-deformed and monotonically strained conditions. It is more pronounced in the monotonically strained material despite the higher starting level. After annealing above 350°C room temperature hardness does not change much, until 500°C. Decrease in hardness at 500°C was around 5 % for both conditions, and reached almost 22 % at 650°C for the monotonically strained material. The cyclically strained material softens at all temperatures, and reaches 30 % decrease after annealing at 600°C, 238 min.

- Hardening was also observed during the low cycle fatigue tests performed around 300°C due to dynamic strain ageing. Cyclic hardening starts rather strongly in the beginning of the fatigue life and then continues with a decreasing rate. At 500°C, cyclic softening can be observed during the entire fatigue life. Hold times showed that the material exhibits stress relaxation due to viscous effects from temperatures around 250–300°C, increasing strongly with temperature. The influence of hold times on the stress-strain loop during further cycling is small.

- Large influence of temperature was observed on the ratcheting behaviour of R7T material. At 300°C, the lowest final ratcheting strain is achieved among the four temperatures tested, due to DSA induced hardening. Fatigue life in the ratcheting tests is longest for the test run at 300°C, while it drops to very low number of cycles to failure at the higher temperatures due to severe softening.

- All biaxial tests exhibit the same initial hardening within the first one or two cycles, but then their behaviour differentiates depending on temperature.Biaxial loading gives much higher strain hardening when compared to uniaxial with the maximum value reaching almost 28 % and an average of 22 % in the testing conditions examined.

- Fatigue life of R7T material is much decreased when the material is subjected to biaxial non proportional loading for comparable equivalent strain amplitudes.

- After heat treatments, the microstructure evaluations showed that pearlite lamellae in the un-deformed R8T material start to break up around 450°C, with more pronounced effect for longer heat treatment durations and higher temperatures.

Pearlite lamellae begin to break up earlier for both pre-strained states at around 400°C. Some regions remain seemingly unaffected by temperature, and deformation localised to certain colonies and free ferrite could be a possible explanation.

- Interlamellar spacing as well as free ferrite content has been measured and found to increase with increasing depth below the running surface of the wheel for both materials studied. As a result of the above, hardness values decrease gradually with increasing depth below the running surface. During the life cycle of a wheel, maintenance such as re-profiling by wheel turning is performed at regular intervals. This means that the hardness of the new surface will be slightly lower than the initial state due to the hardness gradient. However, during run-in, the surface will work harden and residual stresses develop increasing the strength of the surface layer. Based on the observations above and literature on near pearlitic steels, it is believed that the results and conclusions made above are valid not only for the virgin surface region, but through the depth of the wheel tread exposed to mechanical and thermal loads during the wheel's service life.

- Image processing seems very promising for estimating the degree of spheroidisation using SEM images. Further work in implementation and verification is needed to make the method robust.

- Increasing temperature leads to a larger fraction of the material being spheroidised with spheroidisation reaching almost 80 % at 650°C for the prestrained R8T and 70 % for the undeformed R8T (spheroidisation defined as aspect ratio of cementite particles L/W>8).

From the EBSD analysis it can be seen that:

- Large pearlite colonies appear to have orientation gradients due to the initial formation of the pearlite while ferrite grains have a more uniform orientation.

- Spheroidised pearlite colonies appear to obtain a more uniform orientation mostly containing low angle boundaries after spheroidisation.

- Large initial orientation gradients are present in the material in its undeformed state. These are reduced with increasing annealing temperature (drops already at 300°C). Orientation gradients remain rather stable for monotonically strained R8T.

Surface layers of rails are subjected to very high rolling contact loads. These lead to accumulation of large shear strains close to the running surface. With this in mind an attempt to create such shear strains artificially was made and subsequent characterisation of this microstructure was performed. The R260 material investigations showed that:

- The predeformation methodology produces a material with repeatable microstructure and properties.

- The rail field samples show large variability both between the different sample locations on the rail profile, as well as between the rail piece extraction sites.

- The predeformation methodology is able to produce a material that falls within the scatter of the properties seen from the field samples, particularly for the locations that show accumulation of large shear strains.
- The interlamellar spacing, and the thickness of ferrite and cementite lamellae decrease very slowly with the increase of shear strain up to around 1.2, after which a faster decrease has been observed.
- The dislocation structure changes from single, straight dislocation lines and dislocation loops from ferrite/cementite interfaces in the initial state, to dislocation tangles at the highest shear strains. The dislocation density increases from 6×10^{13} m^{-2} in the initial state to 5.3×10^{14} m^{-2} at a shear strain of 1.63. This increase of dislocation density is the key factor behind the increase of local hardness/flow stress with shear strain.
- Good agreement has been found between the calculated flow stress increase quantified from structural parameters and the flow stress increase from microhardness measurement, which is underpinned by a discussion of the two strengthening mechanisms in $\sim$200 nm lamellar structures.

In addition to the studies and conclusions mentioned above the next logical step when it comes to mechanical testing of these materials could be thermo-mechanical fatigue testing. Having the ability to change temperature within a test would give a better approximation of heating phenomena as they occur in the actual application. It would be possible to see how properties are retained at lower and higher temperatures. These could then be correlated with simulation studies involving heating and cooling transitions.

Another interesting aspect with the above knowledge of material behaviour at high temperatures would be to investigate relevant railway practices such as welding or grinding. These induce local heating and phase transformations as well.

6 Acknowledgments

First and foremost, I would like to express my appreciation and gratitude to my supervisor Professor Johan Ahlström, for his continuous support, dedication, patience and encouragement throughout the project. The contribution and input of the reference group members to this project is greatly appreciated.

I would like to thank and acknowledge my co-authors Amir Malakizadi, Knut Andreas Meyer, Ali Esmaeili and Xiaodan Zhang for their contributions and help, as well as numerous discussions about pearlite and other topics throughout this project. Also, all colleagues and friends at the Department of Industrial and Materials Science are gratefully appreciated for their kindness, support and for making every working day a little bit special.

Special thanks to Yiming Yao, Roger Sagdahl and Håkan Millqvist for their help with technical issues.

Last but not least, a big thank you goes to Evangelia and my family back in Greece, especially to my beloved parents Nikolaos Nikas and Evdokia Lazaridou.

References

[1] F. A. M. Alwahdi, A. Kapoor, and F. J. Franklin. Subsurface microstructural analysis and mechanical properties of pearlitic rail steels in service. *Wear* **302**.1-2 (2013), 1453–1460. ISSN: 00431648. DOI: 10.1016/j.wear.2012.12.058. URL: http://dx.doi.org/10.1016/j.wear.2012.12.058.

[2] K. Cvetkovski and J. Ahlström. Characterisation of plastic deformation and thermal softening of the surface layer of railway passenger wheel treads. *Wear* **300**.1-2 (2013), 200–204. ISSN: 00431648. DOI: 10.1016/j.wear.2013.01.094.

[3] K. A. Meyer, M. Ekh, and J. Ahlström. Modeling of kinematic hardening at large biaxial deformations in pearlitic rail steel. *International Journal of Solids and Structures* **130-131** (2018), 122–132. ISSN: 00207683. DOI: 10.1016/j.ijsolstr.2017.10.007.

[4] R. Lundén and B. Paulsson. *Introduction to wheel—rail interface research*. Woodhead Publishing Limited, 2009, pp. 3–33. ISBN: 9781845694128. DOI: 10.1533/9781845696788.1.3.

[5] F. Walther and D. Eifler. Fatigue behaviour of railway wheels at different temperatures. *Materials Testing* **46**.Lm (2004), 158–162.

[6] J. Ahlström and B. Karlsson. Microstructural evaluation and interpretation of the mechanically and thermally affected zone under railway wheel flats. *Wear* **232** (1999), 1–14. ISSN: 00431648. DOI: 10.1016/S0043-1648(99)00166-0.

[7] J. Ahlström and B. Karlsson. Analytical 1D model for analysis of the thermally affected zone formed during railway wheel skid. *Wear* **232**.1 (1999), 15–24. ISSN: 00431648. DOI: 10.1016/S0043-1648(99)00167-2.

[8] R. Andersson et al. Numerical investigation of crack initiation in rails and wheels affected by martensite spots. *International Journal of Fatigue* **114**.May (2018), 238–251. ISSN: 0142-1123. DOI: 10.1016/j.ijfatigue.2018.05.023.

[9] S. Chattopadhyay and C. Sellars. Kinetics of pearlite spheroidisation during static annealing and during hot deformation. *Acta metallurgica* **30** (1982), 157–170. URL: http://www.sciencedirect.com/science/article/pii/0001616082900554.

[10] G. N. Haidemenopoulos et al. Investigation of rolling contact fatigue cracks in a grade 900A rail steel of a metro track. *Fatigue and Fracture of Engineering Materials and Structures* **29**.11 (2006), 887–900. ISSN: 8756758X. DOI: 10.1111/j.1460-2695.2006.01048.x.

[11] U. Olofsson and R. Nilsson. Surface cracks and wear of rail: a full-scale test on a commuter train track. *Proceedings of the Institution of Mechanical Engineers, Part F: Journal of Rail and Rapid Transit* **216**.4 (2002), 249–264. ISSN: 0954-4097. DOI: 10.1243/095440902321029208.

[12] *European standard for Wheels —EN 13262- Product requirements*. Tech. rep. 2009.

[13] Y. Okagata. Design Technologies for Railway Wheels and Future Prospects. *NIPPON STEEL & SUMITOMO METAL TECHNICAL REPORT No. 105* 105 (2013).

[14] K. Mädler and M. Bannasch. Materials used for Wheels on Rolling Stock. *7th World Congress on Railway Research* (2006).

[15] K. Cvetkovski, J. Ahlström, and B. Karlsson. Thermal degradation of pearlitic steels: influence on mechanical properties including fatigue behaviour. *Materials Science and Technology* **27**.3 (2011), 648–654. ISSN: 02670836. DOI: 10.1179/026708310X520538.

[16] B. Vitez and D. Krumes. UIC-recommendations for the use of rail steel grades. *Metalurgija* **44**.2 (2005), 137–140. ISSN: 05435846.

[17] *Railway applications – Track – Rail – Part 1: Vignole railway rails 46 kg / m and above, Svensk standard ss-en 13674-1:2011+a1:2017*. Tech. rep. 2017.

[18] K. Mädler et al. Rail Materials: Alternatives and Limits. *Proceedings of the 8th World Congress on Railway Research (WCRR), May* (2008), 18–22.

[19] D. A. Porter, K. E. Easterling, and Y. Sherif. *Phase Transformations in Metals and Alloys*. Vol. 3. 1. 2009. ISBN: 0412450305. DOI: 10.1146/annurev.ms.03.080173.001551.

[20] H. K. D. H. Bhadeshia and R. W. K. Honeycombe. *Steels–Microstructure and Properties*. 2006, p. 357. ISBN: 0750680849.

[21] A. Marder and B. Bramfitt. The Effect of Morphology on the Strength of Pearlite. *Proceedings of the International Conference on the Strength of Metals and Alloys* **7**.March (1970), 822–823.

[22] N. Guo and Q. Liu. Back-scattered electron imaging combined with EBSD technique for characterization of pearlitic steels. *Journal of Microscopy* **246**.3 (2012), 221–228. ISSN: 00222720. DOI: 10.1111/j.1365-2818.2011.03601.x.

[23] B. Wielke. Thermally activated dislocation movement at plastic deformation. *Czechoslovak Journal of Physics B* **31**.2 (1981), 142–156. URL: http://link.springer.com/article/10.1007%2FBF01959435.

[24] G. Schoeck. The Activation Energy of Dislocation Movement. *Physica Status Solidi (B)* **8**.2 (1965), 499–507. ISSN: 03701972. DOI: 10.1002/pssb.19650080209.

[25] P. S. Follansbee and U. F. Kocks. A constitutive description of copper based on the use of the mechanical threshold stress as an internal state variable. *Acta Materialia* **36**.1 (1998), 81–93.

[26] G. Schoeck. The superposition of thermal activation in dislocation movement. *Physica Status Solidi (a)* **87**.2 (1985), 571–581. ISSN: 00318965, 1521396X. DOI: 10.1002/pssa.2210870220.

[27] M. Hiratani and E. M. Nadgorny. Combined Modelling of Dislocation Motion with thermally activated and Drag-Dependent Stages. *Acta Metall.* **49** (2001), 4337–4346.

[28] O. P. Modi et al. Effect of interlamellar spacing on the mechanical properties of 0 . 65 % C steel. *Materials Characterization* **46** (2001), 347–352.

[29] J. Hyzak and I. Bernstein. The role of microstructure on the strength and toughness of fully pearlitic steels. *Metallurgical Transactions A* **7**.August (1976). URL: http://link.springer.com/article/10.1007/BF02656606.

[30] M. Gensamer et al. The tensile properties of steel. *Transactions of American Society for Metals* **30** (1942), 983–1019.

[31] C. M. Bae, C. S. Lee, and W. J. Nam. Effect of carbon content on mechanical properties of fully pearlitic steels. *Materials Science and Technology* **18**.11 (2002), 1317–1321. ISSN: 0267-0836. DOI: 10.1179/026708302225007556.

[32] K. K. Ray and D. Mondal. Effect of interlamellar spacing on strength of pearlite in annealed eutectoid and hypoeutectoid plain carbon steels. *Acta metallurgica et materialia* **39**.10 (1991), 2201–2208. ISSN: 09567151. DOI: 10.1016/0956-7151(91)90002-I.

[33] S. Suresh. *Fatigue of materials*. 1998. DOI: 10.1016/0261-3069(92)90229-B.

[34] L. Miller and G. Smith. *Tensile Fractures in carbon steels*. 1970. URL: http://www.scopus.com/inward/record.url?eid=2-s2.0-0014872852%7B%5C&%7DpartnerID=tZOtx3y1.

[35] M. Dollar, I. M. Bernstein, and A. W. Thompson. Influence of deformation substructure on flow and fracture of fully pearlitic steel. *Acta Metallurgica* **36**.2 (1988), 311–320. ISSN: 00016160. DOI: 10.1016/0001-6160(88)90008-9.

[36] D. Nikas and J. Ahlström. "Thermal deterioration of railway wheel steels". *Proceedings of the 35th Risø International symposium, Risø, Denmark, p. 411-420*. 2014.

[37] T. B. Massalski. *Binary Alloy Phase Diagrams*. Vol. 2. 1990, p. 3589. ISBN: 087170403X. URL: http://www.amazon.com/Binary-Alloy-Phase-Diagrams-Massalski/dp/087170403X.

[38] M. X. Zhang and P. M. Kelly. The morphology and formation mechanism of pearlite in steels. *Materials Characterization* **60**.6 (2009), 545–554. ISSN: 10445803. DOI: 10.1016/j.matchar.2009.01.001.

[39] Y. L. Tian and R. W. Kraft. Mechanisms of Pearlite Spheroidization. *Metallurgical Transactions A* **18**.August (1987), 1403–1414. ISSN: 03602133. DOI: 10.1007/BF02646654.

[40] C. J. Peters and D. Eifler. Influence of Service Temperatures on the Fatigue Behaviour of Railway Wheel and Tyre Steels. *Materials Testing* **51**.11-12 (Nov. 2009), 748–754. ISSN: 0025-5300. DOI: 10.3139/120.110094. URL: http://www.hanser-elibrary.com/doi/abs/10.3139/120.110094.

[41] J. Ahlström. "LCF Loop shape in near pearlitic steels - Influence of temperature". *Proceedings of 7th International Conference on Low Cycle Fatigue, Aachen*. 2013.

[42] S. D. Mesarovic. Dynamic strain aging and plastic instabilities. *Journal of the Mechanics and Physics of Solids* **43**.5 (1995), 671–700. ISSN: 00225096. DOI: 10.1016/0022-5096(95)00010-G.

[43] A. H. Cottrell and B. A. Bilby. Dislocation Theory of Yielding and Strain Ageing of Iron. *Proceedings of the Physical Society. Section A* **62**.1 (2002), 49–62. ISSN: 0370-1298. DOI: 10.1088/0370-1298/62/1/308. eprint: arXiv:1011.1669v3.

[44] M. Palosaari et al. Static strain aging of stabilized ferritic stainless steels. *Metallurgia Italiana* **104**.9 (2012), 25–28. ISSN: 00260843.

[45] A. Ekrami. High temperature mechanical properties of dual phase steels. *Materials Letters* **59**.16 (2005), 2070–2074. ISSN: 0167577X. DOI: 10.1016/j.matlet.2005.02.018.

[46] L. P. Kubin, Y. Estrin, and C. Perrier. On static strain ageing. *Acta Metallurgica Et Materialia* **40**.5 (1992), 1037–1044. ISSN: 09567151. DOI: 10.1016/0956-7151(92)90081-O.

[47] A. van den Beukel. Theory of the effect of dynamic strain aging on mechanical properties. *Physica Status Solidi (a)* **30**.1 (1975), 197–206. ISSN: 00318965. DOI: 10.1002/pssa.2210300120.

[48] K. Cvetkovski, J. Ahlström, and B. Karlsson. Monotonic and cyclic deformation of a high silicon pearlitic wheel steel. *Wear* **271**.1-2 (2011), 382–387. ISSN: 00431648. DOI: 10.1016/j.wear.2010.10.047.

[49] C. .-.-C. Li and W. C. Leslie. Effects of Dynamic Strain Aging on the Subsequent Mechanical Properties of Carbon Steels. *Metallurgical Transactions A* **9A**.December (1978), 1765–1775. ISSN: 03602133. DOI: 10.1007/BF02663406.

[50] S. L. Mannan. Role of dynamic strain ageing in low cycle fatigue. *Bulletin of Materials Science* **16**.6 (1993), 561–582. ISSN: 02504707. DOI: 10.1007/BF02757656.

[51] A. J. Wilkinson and D. Randman. Determination of elastic strain fields and geometrically necessary dislocation distributions near nanoindents using electron back scatter diffraction. *Philosophical Magazine* **90**.9 (2010), 1159–1177. ISSN: 1478-6435. DOI: 10.1080/14786430903304145.

[52] T. Takahashi, D. Ponge, and D. Raabe. Investigation of orientation gradients in pearlite in hypoeutectoid steel by use of orientation imaging microscopy. *Steel Research International* **78**.1 (2007). URL: http://dierk-raabe.com/app/download/5790853628/steel+research+int.+78+(2007)+perlite+texture.pdf.

[53] C. Moussa et al. About quantitative EBSD analysis of deformation and recovery substructures in pure Tantalum. *IOP Conference Series: Materials Science and Engineering* **89**.1 (2015), 012038. ISSN: 1757899X. DOI: 10.1088/1757-899X/89/1/012038.

[54] S. I. Wright, M. M. Nowell, and D. P. Field. M icroscopy M icroanalysis A Review of Strain Analysis Using Electron Backscatter Diffraction. *Microscopy and Microanalysis* **17**.03 (2011), 316–329. ISSN: 1431-9276. DOI: 10.1017/S1431927611000055.

[55] G. Krauss. *STEELS Processing, structure and performance*. 2005. ISBN: 978-0-12-732951-2. DOI: 10.1037/023990.

[56] S. Chattopadhyay and C. M. Sellars. Quantitative measurements of pearlite spheroidization. *Metallography* **10**.1 (1977), 89–105. ISSN: 00260800. DOI: 10.1016/0026-0800(77)90044-1.

[57] N. Nutal et al. Image analysis of pearlite spheroidization based on the morphological characterization of cementite particles. *Image Analysis and Stereology* **29**.2 (2010), 91–98. ISSN: 18545165. DOI: 10.5566/ias.v29.p91-98.

[58] D. Nikas, J. Ahlström, and A. Malakizadi. Mechanical properties and fatigue behaviour of railway wheel steels as influenced by mechanical and thermal loadings. *Wear* **366-367** (2016), 407–415. ISSN: 00431648. DOI: 10.1016/j.wear.2016.04.009. URL: http://dx.doi.org/10.1016/j.wear.2016.04.009.

[59] H. Chen and L. X. Cai. Theoretical Conversions of Different Hardness and Tensile Strength for Ductile Materials Based on Stress–Strain Curves. *Metallurgical and Materials Transactions A: Physical Metallurgy and Materials Science* **49**.4 (2018), 1090–1101. ISSN: 10735623. DOI: 10.1007/s11661-018-4468-8.

[60] X. Zhang et al. Hierarchical structures in cold-drawn pearlitic steel wire. *Acta Materialia* **61**.13 (2013), 4898–4909. ISSN: 13596454. DOI: 10.1016/j.actamat.2013.04.057.

[61] C. Zhang, Y. Liu, and L. Zhou. Transformation Conditions - Microstructures - Mechanical Properties Relationship in 0.60%C Hypoeutectoid Steel. *Steel Research International* **82**.10 (Oct. 2011), 1207–1212. ISSN: 16113683. DOI: 10.1002/srin.201100075. URL: http://doi.wiley.com/10.1002/srin.201100075.

[62] M. Guziewski, S. P. Coleman, and C. R. Weinberger. Atomistic investigation into the mechanical properties of the ferrite-cementite interface: The Bagaryatskii orientation. *Acta Materialia* **144** (2018), 656–665. ISSN: 13596454. DOI: 10.1016/j.actamat.2017.10.070.

[63] D. Nikas, X. Zhang, and J. Ahlström. Evaluation of local strength via microstructural quantification in a pearlitic rail steel deformed by simultaneous compression and torsion. *Under review for international publication* (2018).